








## Nanostructure and phase engineering of manganese oxide thin films grown by pulsed laser deposition: A Raman and XRD study

Andrea Macrelli <sup>1,\*</sup>, Arianna Monforte Ferrario <sup>1</sup>, Alessio Lamperti <sup>2</sup>, Alberto Calloni <sup>3</sup>, Valeria Russo <sup>1</sup>,  
Carlo S. Casari <sup>1</sup> and Andrea Li Bassi <sup>1,†</sup>

<sup>1</sup>*Micro and Nanostructured Materials Lab (NanoLab), Department of Energy, Politecnico di Milano, Via G. Ponzio 34/3, 20133 Milano, Italy*

<sup>2</sup>*Institute for Microelectronics and Microsystems (IMM), Consiglio Nazionale delle Ricerche (CNR), Unit of Agrate Brianza, Via C. Olivetti 2, 20864 Agrate Brianza, Italy*

<sup>3</sup>*Department of Physics, Politecnico di Milano, Piazza Leonardo da Vinci 32, 20133 Milano, Italy*



(Received 13 May 2023; accepted 31 July 2023; published 25 August 2023)

Manganese, showing stable oxidation states spanning from +2 to +7, gives rise to a variety of oxides ( $\text{MnO}_x$ ) whose exploitation in several technological fields, such as energy conversion and storage, catalysis, sensing, and environmental and biomedical engineering, is highly promising. Nevertheless, the chemical complexity and the structural richness of  $\text{MnO}_x$ —involving mixed-valence and metastable species—make the correct identification by Raman spectroscopy challenging, further complicated by the laser sensitivity, poor Raman activity, and conflicting literature scenario. Moreover, a careful optimization of the material in terms of phase, structure, and morphology is highly desirable in view of the final application, where precise control over the materials properties is essential. In this paper, we discuss the capability of room-temperature pulsed laser deposition (PLD) followed by postdeposition thermal treatments to successfully grow engineered and pure  $\text{MnO}_x$  thin films, whose phase and morphology at the nanoscale can be totally decoupled and independently optimized. The detailed Raman characterization of these films enabled a clear identification of specific  $\text{MnO}_x$  phases and poses the basis for the rationale of the  $\text{MnO}_x$  Raman spectra. Starting from the same  $\text{MnO}$  PLD target, we obtained five different  $\text{MnO}_x$  phases (i.e.,  $\text{MnO}$ ,  $\text{Mn}_3\text{O}_4$ ,  $\text{Mn}_2\text{O}_3$ , amorphous  $\text{MnO}_2$ , and  $\alpha$ - $\text{MnO}_2$ ) with tailored and tunable degree of porosity and crystallinity, by modulating process parameters like the  $\text{O}_2$  deposition partial pressure (vacuum to 100 Pa), the type of substrate, and the annealing temperature (300–900 °C) and atmosphere (air/vacuum). The Raman spectroscopy reliability of the  $\text{MnO}_x$  phase assignment was assessed by thoroughly investigating the impact of the exciting laser power, and it was further validated by energy-dispersive x-ray spectroscopy, x-ray photoemission spectroscopy, and x-ray diffraction, providing additional insight into the compositional properties and the crystalline structure.

DOI: [10.1103/PhysRevMaterials.7.083403](https://doi.org/10.1103/PhysRevMaterials.7.083403)

### I. INTRODUCTION

Manganese oxides ( $\text{MnO}_x$ ) are a class of inorganic compounds which can be applied in different technological fields, including electrochemical energy storage, catalysis, and sensing [1–4]. As Mn exists with several stable oxidation states in the range +2 to +7 (with +2, +3, and +4 states being the most common ones), several Mn oxides occur naturally and can be synthesized in a laboratory. For example, manganosite  $\text{MnO}$  exhibits a rock-salt structure, with close-packed  $\text{Mn}^{2+}$  cations and  $\text{O}^{2-}$  anions [5,6]. Mn sesquioxide  $\text{Mn}_2\text{O}_3$  contains  $\text{Mn}^{3+}$  cations and crystallizes in either a body-centered cubic ( $\alpha$ - $\text{Mn}_2\text{O}_3$ , bixbyite) or a metastable tetragonal ( $\gamma$ - $\text{Mn}_2\text{O}_3$ ) phase [5]. Hausmannite  $\text{Mn}_3\text{O}_4$  is a mixed-valence oxide with normal spinel structure, where  $\text{Mn}^{2+}$  cations reside in the tetrahedral sites, while  $\text{Mn}^{3+}$  occupy the octahedral ones. Because of the presence of octahedrally coordinated  $\text{Mn}^{3+}$  cations,  $\text{Mn}_3\text{O}_4$  is a tetrag-

onal spinel oxide due to the cooperative Jahn-Teller (JT) distortion of the  $[\text{Mn}^{3+}\text{O}_6]$  octahedra in the crystal [5,6]. Finally, Mn dioxide  $\text{MnO}_2$  contains  $\text{Mn}^{4+}$  cations arranged in  $[\text{Mn}^{4+}\text{O}_6]$  octahedra. Depending on the relative arrangement of  $[\text{Mn}^{4+}\text{O}_6]$  octahedra in the crystal structure, several  $\text{MnO}_2$  polymorphs exist, exhibiting a tunneled ( $\alpha$ ,  $\beta$ , R,  $\gamma$ , T), layered ( $\delta$ ), or spinel ( $\lambda$ ) structure [5,7]. In addition, metastable oxides containing Mn cations with different oxidation states in variable amounts, such as  $\text{Mn}_5\text{O}_8$  [8], and oxyhydroxide phases ( $\alpha$ - and  $\gamma$ - $\text{MnOOH}$ ) [5] exist. The structural, catalytic, electrical, electrochemical, optical, and magnetic properties, as well as the chemical stability, differ significantly among the various  $\text{MnO}_x$  phases/polymorphs and are strongly affected by their specific micro/nanostructure. Therefore, precise control over their phase, structure, and morphology is highly desirable in view of exploitation on advanced technology applications. In this context, the possibility of distinguishing among different phases is fundamental, especially when chemical or electrochemical reactions occur, leading to structural transformation and chemical conversion. X-ray diffraction (XRD) and x-ray photoelectron spectroscopy (XPS) are common techniques conventionally used to

\*Corresponding author: [andrea.macrelli@polimi.it](mailto:andrea.macrelli@polimi.it)

†Corresponding author: [andrea.libassi@polimi.it](mailto:andrea.libassi@polimi.it)

discriminate different Mn compounds [7]. In addition, Raman spectroscopy has been extensively employed; however, the spectral assignment is rather complex compared with other oxide families [5,6,9]. First, the Raman activity of several Mn oxides is weak. Secondly, most Mn oxides are low-band-gap materials and are sensitive to laser irradiation during Raman measurements, as photoinduced damage may lead to localized amorphization, oxidation, and/or formation of metastable secondary phases, especially at high laser intensity and for long acquisition times. Thirdly, Mn oxides can be synthesized following a wide variety of chemical and physical routes, which affect in a nonnegligible way the average Mn oxidation state, the number of defects, the oxygen stoichiometry, and the type of stabilizing cations/molecules trapped in the Mn oxide crystal structure. This effect is even more relevant for natural Mn oxides. As a result, reported Raman spectra for different Mn oxides—even recently—are conflicting and do not allow for an unambiguous assignment to  $\text{MnO}_x$  phases [5–7,9–12]. Pure phase  $\text{MnO}_x$  thin films, with controlled stoichiometry and structure, can act as useful systems for the analysis of the Raman behavior of different phases.

Several physical and chemical synthesis techniques have been employed to produce  $\text{MnO}_x$  films, including magnetron sputtering [13–15], atomic layer deposition (ALD) [16–19], thermal evaporation [20,21], pulsed laser deposition (PLD) [22–27], spray pyrolysis [28], plasma-enhanced chemical vapor deposition [29], molecular beam epitaxy [30], sol-gel processes [31,32], successive ionic layer adsorption and reaction [33], hydrothermal reaction, and electrodeposition [32,34,35]. PLD is an effective physical technique exploiting ablation of a target by intense laser pulses to grow thin films on a proper substrate. The control of deposition parameters like the background pressure during deposition and the substrate temperature allows varying the Mn oxidation state and hence the  $\text{MnO}_x$  phase. Since PLD leads to a nonequilibrium film growth, metastable  $\text{MnO}_x$  phases can also be produced [22,26]. For example, Neubeck *et al.* [22] produced epitaxial MnO thin films from a  $\text{Mn}_2\text{O}_3$  target on sapphire (001) and MgO (111) using a Nd:YAG laser ( $\lambda = 532$  nm), depositing in vacuum ( $1 \times 10^{-2}$  Pa), and with the substrate at 700 °C. Isber *et al.* [25] investigated the effect of oxygen pressure (1.3, 6.5, and 13 Pa) and substrate temperature (550–800 °C) on films grown by the ablation of a MnO target, highlighting a phase transition from  $\text{Mn}_2\text{O}_3$  to  $\text{Mn}_3\text{O}_4$  at 700 °C. Yang [23] employed PLD to produce amorphous  $\text{MnO}_x$ ,  $\text{Mn}_2\text{O}_3$ , and  $\text{Mn}_3\text{O}_4$  thin films for supercapacitor applications, starting from either a  $\text{Mn}_3\text{O}_4$  or a metallic Mn target, and varying both substrate temperature (20–750 °C) and oxygen pressure (0–67 Pa). Similarly, Xia *et al.* [24] prepared MnO,  $\text{Mn}_3\text{O}_4$ , and  $\text{Mn}_2\text{O}_3$  thin films for lithium microbatteries by PLD at 600 °C and in vacuum, 26.7 Pa, and 93.3 Pa of oxygen, respectively, from a metallic Mn target. Notably, none of the previous authors reported the synthesis of crystalline  $\text{MnO}_2$  polymorphs by PLD [22–25]. Indeed, Garten *et al.* [26] made use of a high-throughput experimental combinatorial research and showed how the  $\text{MnO}_2$  phase could not be obtained by PLD for any combination of total and oxygen pressure ( $1.3 \times 10^{-3}$  to 13.3 Pa), substrate temperature (250–550 °C), and type of target (MnO,  $\text{Mn}_2\text{O}_3$ , or  $\text{MnO}_2$ ). As indicated also by Yang [23], amorphous  $\text{MnO}_x$  phases obtained at low substrate tem-

perature ( $< 300$  °C) could be identified as amorphous  $\text{MnO}_2$ . The synthesis of crystalline  $\text{MnO}_2$  by PLD was reported by Tabbal *et al.* [36] to occur only in a narrow experimental range (500 °C, 33.3–66.6 Pa of oxygen) during the ablation of a MnO target. A strategy to promote the formation of  $\beta$ - $\text{MnO}_2$  and  $\gamma$ - $\text{MnO}_2$  phases with good crystalline quality at low substrate temperature was suggested by Abi-Akl *et al.* [37] and consisted of growing thin films by PLD in a highly reactive atmosphere of remote oxygen plasma. Isber *et al.* [25], Xia *et al.* [24], Yang [23], Garten *et al.* [26], Tabbal *et al.* [36], and Abi-Akl *et al.* [37] all made use of a KrF excimer laser ( $\lambda = 248$  nm).

Herein, we present room-temperature PLD, combined with postdeposition thermal annealing either in air or in vacuum, as an effective technique to synthesize pure  $\text{MnO}_x$  phases, starting from the same MnO target and adjusting the deposition and annealing parameters. This approach allowed us to decouple the film phase from its nanostructure, thus enabling the fine tuning of the film properties and the achievement of a rationally designed  $\text{MnO}_x$  material. As-deposited and annealed  $\text{MnO}_x$  films were then characterized by Raman spectroscopy, XPS, and XRD, and the results were employed to assess the open issue of the unique assignment of Raman spectra to each specific Mn oxide phase.

## II. MATERIALS AND METHODS

### A. Synthesis of $\text{MnO}_x$ thin films

$\text{MnO}_x$  thin films were grown on silicon (100) substrates (Siegert Wafer) by PLD, using an experimental apparatus already described elsewhere [38,39]. Briefly, a MnO vacuum hot-pressed target (99.9% purity, Testbourne B.V.) was ablated by nanosecond laser pulses from a Nd:YAG laser source (second harmonic,  $\lambda = 532$  nm, repetition rate 10 Hz, pulse duration 5–7 ns). Concomitant target rotation and translation ensured a uniform ablation. Laser pulses were focused by a plano-convex lens and reached the target surface with an incidence angle of 45°, corresponding to an elliptical spot size of  $\sim 6$  mm<sup>2</sup> and a resultant laser fluence of  $\sim 2$  J cm<sup>-2</sup> (pulse energy  $\sim 120$  mJ pulse<sup>-1</sup>). Depositions were carried out at room temperature in a stainless-steel vacuum chamber, equipped with a primary scroll pump connected in series to a turbomolecular pump. After reaching the base pressure ( $1\text{--}4 \times 10^{-3}$  Pa), deposition was performed either in vacuum or in O<sub>2</sub> gas atmosphere (Sapio, 99.999% purity), whose pressure was regulated by mass flow controllers at 1, 10, 50, and 100 Pa. Silicon substrates were mounted on a rotating holder at a constant substrate-to-target distance of 5 cm, and the deposition time was set to 20 min. Thermal treatments in air were performed in the temperature range 300–900 °C using a Lenton Muffle furnace (4 °C min<sup>-1</sup> heating ramp). Annealing in vacuum was carried out at 500 °C in a homemade furnace, equipped with a high-vacuum chamber (base pressure  $\sim 4.5 \times 10^{-5}$  Pa, 10 °C min<sup>-1</sup> heating ramp). The dwell time at the nominal annealing temperature was set to 2 h for 500 and 900 °C in air, 4 h for 300 °C in air, and 1 h for 500 °C in vacuum. For comparison, additional  $\text{MnO}_x$  films were grown by PLD in equal conditions also on soda-lime glass slides (Marienfeld) and F-doped SnO<sub>2</sub> (FTO)-coated

glass slides (Sigma Aldrich), adjusting the deposition time to achieve a nominal film thickness of  $\sim 500$  nm. Thermal annealing in the presence of  $\text{Na}^+$  cations—as will be clarified in Sec. IV E—was performed in air at  $500^\circ\text{C}$  for 2–5 h using 20  $\mu\text{L}$  droplets of  $\text{Na}_2\text{SO}_4$  0.2 M aqueous solution, prepared from deionized water and anhydrous sodium sulphate (Sigma Aldrich,  $\geq 99.0\%$  purity). In view of XPS measurements, selected films were grown on Pt-coated Si substrates or Ti foil (Sigma Aldrich), with a nominal thickness of  $\sim 150$  nm.

### B. Characterization

Top-view and cross-sectional morphological images of  $\text{MnO}_x$  thin films were acquired using a field emission scanning electron microscope (FE-SEM, Zeiss SUPRA 40), equipped with a Peltier-cooled silicon drift detector (Oxford Instruments) for energy-dispersive x-ray spectroscopy (EDXS) measurements. EDXS was employed to evaluate the film composition through the AZtec EDS software, with an accelerating voltage of 10 kV. Raman analysis was performed using a Renishaw InVia micro-Raman spectrometer, equipped with a diode-pumped solid-state laser ( $\lambda = 532$  nm) and with an 1800 grooves  $\text{mm}^{-1}$  grating. The laser was focused on the sample using a  $50\times$  objective, and the incident power on the sample was varied in the range 0.70–8.75 mW to appraise the threshold for laser-induced degradation. Unless otherwise specified, each spectrum was acquired using 200 accumulations, 1 s each. Systematic fitting analysis of all Raman spectra was performed by means of Lorentzian functions. XPS measurements were performed in an ultrahigh vacuum system (base pressure in the high  $10^{-9}$  Pa range) described in detail in Ref. [40]. Photoelectrons were excited by Al  $K\alpha$  radiation ( $h\nu = 1486.6$  eV) and detected by means of a 150 mm hemispherical analyzer operated at a pass energy of 20 eV, yielding an overall full width at half-maximum (FWHM) resolution of  $\sim 0.9$  eV. Source satellites have been subtracted from the raw data. The binding energy (BE) scale has been corrected by setting the photoemission feature from C 1s adventitious carbon at the surface to 284.6 eV, as in Ref. [41]. The information depth of XPS is of the order of magnitude of the inelastic mean free path of the photoelectrons, which is  $\sim 3$  nm for Mn oxides [42]. The crystalline structure of  $\text{MnO}_x$  films was probed by XRD in grazing incidence configuration (GIXRD), with an incidence angle of  $\omega = 2^\circ$ . GIXRD measurements were performed with a HRD3000 diffractometer (Ital Structures, Riva del Garda, Italy) operating with monochromated Cu  $K\alpha$  radiation ( $\lambda = 0.1541$  nm) and equipped with a curved position-sensitive multichannel gas-filled detector ( $2\theta$  range 0– $120^\circ$ , resolution  $0.029^\circ$ , Inel CPS-120). Rietveld refinement of selected GIXRD patterns was performed using MAUD software [43]. UV-Vis optical transmittance of selected  $\text{MnO}_x$  films was probed by a Shimadzu UV-1800 spectrophotometer in the wavelength range 190–1100 nm.

## III. OVERVIEW OF CRYSTAL STRUCTURES AND RAMAN SPECTRA OF Mn OXIDES

Despite the concerns outlined in the Introduction about the characterization and unique phase identification of Mn oxides

by Raman spectroscopy, we provide here a general overview about the Raman spectra of selected  $\text{MnO}_x$  phases reported in previous studies, especially for those of interest in this paper. Additional details about Mn oxide and oxyhydroxide phases, including the mineralogic name, the crystal symmetry, and the space group, can be found in Table I, which also summarizes the main Raman peaks of each  $\text{MnO}_x$  phase according to literature. For an extensive comparison about the Raman assignment of  $\text{MnO}_x$  phases, we refer to Table SI in the Supplemental Material [44].

### A. Manganosite MnO

Manganosite MnO possesses a cubic close-packed NaCl structure (space group  $Fm\bar{3}m$ ); therefore, no Raman active modes are expected by factor group analysis. However, defects and local distortions in the crystal structure can induce Raman activity [6]. It is worth mentioning that MnO tends to be highly sensitive to the Raman excitation laser beam since it may cause the localized oxidation and transformation of the material into a spinellike phase [5,6], depending on its power and wavelength. Based on the spectra reported in preceding works [5,6,45–47], the main defect-induced Raman features of MnO correspond to two broad and asymmetric bands centered at 523–535 and 1050  $\text{cm}^{-1}$ : the former has been previously assigned to Mn–O stretching mode of  $\text{Mn}^{2+}$  cations in cubic arrangement [5], 2TO, or LO phonons [46], while the latter originates from the envelop of the TO + LO band with the 2LO modes [45,46]. On the contrary, the peak sometimes reported at 650–660  $\text{cm}^{-1}$  is likely associated with the laser-induced formation of  $\text{Mn}_3\text{O}_4$  or other metastable spinellike phases [6,47]. For comparison, the Raman spectrum of our pristine, not-ablated PLD MnO target is reported in the Supplemental Material (Fig. S1) [44], showing the characteristic MnO bands (535 and 1042  $\text{cm}^{-1}$ ) in addition to the peak at 653  $\text{cm}^{-1}$  related to the localized formation of hausmannite (see Sec. III B) under the Raman laser beam.

### B. Hausmannite $\text{Mn}_3\text{O}_4$

Hausmannite  $\text{Mn}_3\text{O}_4$  (or  $\text{MnMn}_2\text{O}_4$ ) is a normal tetragonal spinel containing Mn cations in both +2 and +3 oxidation state, in which the  $\text{Mn}^{3+}$  cations in octahedral coordination are responsible for the cooperative JT effect leading to the distortion of the spinel crystal from cubic ( $Fd\bar{3}m$ ) to tetragonal ( $I4_1/amd$ ) [50].  $\text{Mn}^{2+}$  cations instead reside in tetrahedral sites. Factor group analysis predicts 10 Raman-active modes for  $\text{Mn}_3\text{O}_4$  ( $\Gamma = 2A_{1g} + 3B_{1g} + B_{2g} + 4E_g$ ) [50,65,66]; however, the Raman spectrum is dominated by a sharp  $A_{1g}$  peak centered at  $\sim 660$   $\text{cm}^{-1}$ , which is typical of all spinel oxides [51] and could be assigned to the  $\text{Mn}^{2+}$ –O stretching vibrations in  $[\text{Mn}^{2+}\text{O}_4]$  tetrahedra [5,7,51]. It is worth mentioning that this assignment is not unique and—e.g., see Malavasi *et al.* [50]—the main  $A_{1g}$  Raman peak is ascribed to the motion of oxygen atoms in  $[\text{Mn}^{3+}\text{O}_6]$  octahedra. Less intense Raman peaks are located at  $\sim 320$   $\text{cm}^{-1}$  (Mn–O bending mode in  $[\text{Mn}^{3+}\text{O}_6]$  octahedra,  $A_{1g}$  symmetry [7,66]) and  $\sim 370$   $\text{cm}^{-1}$  (Mn–O–Mn asymmetric stretching mode,  $B_{2g}$  symmetry [66]). Very weak bands can also be detected at  $\sim 290$ , 388, and 480  $\text{cm}^{-1}$ , assigned to  $B_{1g}$  and/or  $E_g$  modes [6,66].

TABLE I. Details about Mn oxides and oxyhydroxides, including the main Raman peaks according to the literature (because of the wide discrepancy across different references for the same  $\text{MnO}_x$  phase, we have selected the values appearing more coherent; in addition, when slightly different values were found in separate works, they are reported as ranges).

Formula	Mineral name	Crystal system	Space group	Mn valence	Additional information	Main Raman peaks from literature ( $\text{cm}^{-1}$ )
MnO	Manganosite	Cubic	$Fm\bar{3}m$	+2	NaCl-type structure	[5,6] 523–535, 1050 [5,6,45–47]
$\alpha$ - $\text{Mn}_2\text{O}_3$	Bixbyite	Cubic	$Ia\bar{3}$	+3	Body-centered cubic structure (C-type)	[5,7] 195–200, 310–320, 640–650, 700–703 [7,9,48]
$\gamma$ - $\text{Mn}_2\text{O}_3$	–	Tetragonal	$I4_1/amd$	+3	Distorted spinel metastable phase	[5,49] 628 [5]
$\text{Mn}_3\text{O}_4$	Hausmannite	Tetragonal	$I4_1/amd$	+2/+3 (+2.7)	Normal tetragonal spinel due to JT effect	[5,6] 320, 370, 654–660 [5,7,50,51]
$\alpha$ - $\text{MnO}_2$	Hollandite	Tetragonal	$I\bar{4}/m$	+4	Body-centered tetragonal structure ( $2 \times 2$ ) tunnels	[5,52] 180–185, 573–583, 632–649 [52–55]
$\beta$ - $\text{MnO}_2$	Pyrolusite	Tetragonal	$P4_2/mnm$	+4	Rutile-type structure ( $1 \times 1$ ) tunnels	[5,52] 532–538, 661–667 [5–7,9,52]
R- $\text{MnO}_2$	Ramsdellite	Orthorhombic	$Pbnm$	+4	( $1 \times 2$ ) tunnels	[5,9] 518–520, 575–580, 630 [5]
$\gamma$ - $\text{MnO}_2$	Nsutite	Hexagonal	–	+4	Random intergrowth of $\beta$ - and R- $\text{MnO}_2$ ( $1 \times 2$ )+(2 $\times$ 2) tunnels	[7,56] 572–582, 654–658 [7,56]
$\delta$ - $\text{MnO}_2$	Birnessite	Monoclinic	$C2/m$	+4	Layered structure	[7,57] 500–510, 565–585, 625–650 [7,57]
$\varepsilon$ - $\text{MnO}_2$	Akhtenskite	Hexagonal	$P6_3/mmc$	+4	Dense stack	[1,58] NA –
$\lambda$ - $\text{MnO}_2$	–	Cubic	$Fd\bar{3}m$	+4	3D network of interconnected ( $1 \times 1$ ) tunnels cubic-close-packed spinel structure ( $3 \times 3$ ) tunnels	[5,59] 596 [5,59]
T- $\text{MnO}_2$	Todorokite	Monoclinic	$P2_1/m$	+4	Layered structure metastable phase	[1,60] 641 [5]
$\text{Mn}_5\text{O}_8$	–	Monoclinic	$C2/m$	+2/+4 (+3.2)	Isostructural to R- $\text{MnO}_2$	[8,61] 262–264, 647–648 [8,61]
$\alpha$ - $\text{MnOOH}$	Groutite	Orthorhombic	$Pbnm$	+3	Isostructural to $\beta$ - $\text{MnO}_2$	[9] 142, 352, 384, 528, 552, 615 [5]
$\gamma$ - $\text{MnOOH}$	Manganite	Monoclinic	$P2_1/c$	+3	Isostructural to $\beta$ - $\text{MnO}_2$	[7,9] 147, 358, 388, 531–533, 557–558, 621–623 [6,7,9,12]
$\text{Mn}(\text{OH})_2$	Pyrochroite	Rhombohedral	$P\bar{3}m1$	+2	Layered structure	[62,63] 470 [64]

$\text{Mn}_3\text{O}_4$  is highly stable under the laser beam [5], and no photoinduced damage is typically detected.

### C. Bixbyite $\alpha$ - $\text{Mn}_2\text{O}_3$

Bixbyite  $\alpha$ - $\text{Mn}_2\text{O}_3$  is the stable polymorph of Mn sesquioxide and has a body-centered cubic structure with two nonequivalent sites for  $\text{Mn}^{3+}$  cations [5,7]. Mn atoms are arranged in a close-packed lattice, with  $\text{O}^{2-}$  ions occupying  $\frac{3}{4}$  of the tetrahedral interstitial sites, leading to  $Ia\bar{3}$

symmetry [67,68]. The cubic structure of  $\alpha$ - $\text{Mn}_2\text{O}_3$  is stable  $> 302$  K (i.e.,  $\sim 29$  °C), whereas at lower temperature, a transition to an orthorhombic structure (space group  $Pbca$ ) occurs, even if the distortion of the cubic symmetry is small ( $\sim 0.8\%$ ) [68]. Factor group analysis predicts 22 Raman-active modes for  $\alpha$ - $\text{Mn}_2\text{O}_3$  ( $\Gamma = 4A_g + 4E_g + 14T_g$ ) [69]. Some discrepancies—even in the most recent literature—are observed across the Raman spectra of  $\alpha$ - $\text{Mn}_2\text{O}_3$ . Julien *et al.* [5] ( $\lambda_{\text{ex}} = 514.5$  nm) and Bernardini *et al.* [6,70] identified a strong peak at  $\sim 580$ – $592$   $\text{cm}^{-1}$  as the main Raman feature of

bixbyite, corresponding to the  $\text{Mn}^{3+}-\text{O}$  stretching vibration. The same peak at  $581\text{ cm}^{-1}$  is also present in the Raman spectrum provided by Bernard *et al.* [12] ( $\lambda_{\text{ex}} = 514.5\text{ nm}$ ), although the overall spectral shape is different from Ref. [5]. On the other hand, no strong peaks at  $\sim 580\text{ cm}^{-1}$  can be detected in the Raman spectra of  $\alpha\text{-Mn}_2\text{O}_3$  reported by White and Keramidis [69] ( $\lambda_{\text{ex}} = 488$  and  $514.5\text{ nm}$ ), Kapteijn *et al.* [48] ( $\lambda_{\text{ex}} = 514.5\text{ nm}$ ), Buciuman *et al.* [11] (who also highlighted the effect on the Raman spectra of three different excitation wavelengths, i.e.,  $\lambda_{\text{ex}} = 647.1, 514.5,$  and  $457.9\text{ nm}$ ), Gao *et al.* [52] ( $\lambda_{\text{ex}} = 632.8\text{ nm}$ ), Post *et al.* [9] ( $\lambda_{\text{ex}} = 632.8\text{ nm}$ ), and Xin *et al.* [7] ( $\lambda_{\text{ex}} = 532\text{ nm}$ ). In addition to obvious discrepancies regarding the exact peak position and relative intensity ratios, the Raman spectra of  $\alpha\text{-Mn}_2\text{O}_3$  reported in Refs. [7,9,11,48,52,69] are closely similar and, interestingly, also match the spectrum presented in Ref. [5] if the peak at  $592\text{ cm}^{-1}$  is excluded. The differences in the Raman spectra of bixbyite can be explained as follows: (i) the Raman signal of  $\alpha\text{-Mn}_2\text{O}_3$  is very weak, and the material tends to decompose quickly if the laser power is increased [11,69]; (ii) other metastable polymorphs of  $\text{Mn}_2\text{O}_3$  exist (e.g.,  $\gamma\text{-Mn}_2\text{O}_3$  [5]), whose presence in traces may complicate the overall spectrum; (iii) impurities, especially in natural samples, may exist; indeed, according to Post *et al.* [9], a strong feature at  $\sim 575\text{--}585\text{ cm}^{-1}$  could be ascribed to ramsdellite ( $\text{R-MnO}_2$ ) or other  $\text{MnO}_2$  polymorph intergrowths. All things considered, taking the spectra reported in Refs. [7,9] as a reference, the Raman spectrum of  $\alpha\text{-Mn}_2\text{O}_3$  is characterized by strong peaks at  $\sim 700\text{--}703, \sim 640\text{--}650, \sim 310\text{--}320,$  and  $\sim 195\text{--}200\text{ cm}^{-1}$ , in addition to weak bands at  $\sim 126, 480,$  and  $540\text{--}545\text{ cm}^{-1}$ .

#### D. $\text{MnO}_2$ polymorphs

Mn dioxide can exist in several polymorphic forms (at least eight), depending on the relative organization and space orientation of  $[\text{Mn}^{4+}\text{O}_6]$  octahedra. In addition to the issues highlighted above (i.e., instability under the laser beam and presence of impurities), the Raman characterization of  $\text{MnO}_2$  species is complicated by both the presence of stabilizing cations in the tunneled/layered structure and the coexistence of multiple polymorphs, which affects in a nonnegligible way the final spectrum. Herein, for the sake of simplicity, we discuss the state-of-the-art Raman spectra of four main  $\text{MnO}_2$  polymorphs, i.e.,  $\alpha, \beta, \gamma,$  and  $\delta$ .

##### 1. Hollandite $\alpha\text{-MnO}_2$

Here,  $\alpha\text{-MnO}_2$  is a tunneled  $\text{MnO}_2$  polymorph exhibiting a body-centered tetragonal structure (space group  $I\bar{4}/m$ ) and comprising  $(2 \times 2)$  and  $(1 \times 1)$  tunnels, where the  $(n \times n)$  notation defines the number of octahedral units involved in each side of the tunnel. Typically, the large  $(2 \times 2)$  tunnels, with a size of  $(4.6 \times 4.6\text{ \AA})$ , host metallic cations that help stabilizing the structure, especially in chemically synthesized  $\alpha\text{-MnO}_2$ , while the  $(1 \times 1)$  tunnels are empty [52]. The term *hollandite* may refer either to all  $\text{MnO}_2$  polymorphs exhibiting a  $(2 \times 2)$  tunnel structure or to a specific  $\text{Ba}^{2+}$ -intercalated  $\alpha\text{-MnO}_2$  material. Other cation-intercalated materials with a hollandite-type structure are cryptomelane ( $\text{K}^+$ ), coronadite ( $\text{Pb}^{2+}$ ), and manjiroite ( $\text{Na}^+$ ) [5,9]. Structural deviations

from the ideal tetragonal structure may lead to monoclinic symmetry ( $C2/m$ ) [6]. The Raman spectrum of  $\alpha\text{-MnO}_2$  is sensitive to the chemical species in the tunnels; however, some fingerprint features can be identified. Based on the spectra reported in Refs. [52–55], the Raman spectrum of  $\alpha\text{-MnO}_2$  is characterized by a strong and sharp peak at  $\sim 180\text{--}185\text{ cm}^{-1}$  ( $A_g$  symmetry), by a couple of bands at  $\sim 573\text{--}583$  and  $\sim 632\text{--}649\text{ cm}^{-1}$  ( $A_g$  symmetry), and by weaker peaks at  $\sim 330$  ( $A_g$  symmetry),  $385$  ( $B_g$  symmetry), and  $510\text{ cm}^{-1}$ . Here,  $A_g$  symmetry modes originate from the breathing vibrations of  $[\text{Mn}^{4+}\text{O}_6]$  octahedra in the tetragonal framework [52].

##### 2. Pyrolusite $\beta\text{-MnO}_2$

Here,  $\beta\text{-MnO}_2$  with a tetragonal rutile-type structure (space group  $P4_2/mnm$ ) is the thermodynamically stable  $\text{MnO}_2$  polymorph [5]. It is constituted by  $(1 \times 1)$  tunnels which, considering the small  $2.3 \times 2.3\text{ \AA}$  size, are normally empty [52]. Pyrolusite is highly sensitive to heating and laser irradiation [6]; therefore, attention should be paid in the correct interpretation of its Raman spectrum. According to Ref. [52], four Raman-active modes are allowed for  $\beta\text{-MnO}_2$ , which has low Raman activity and normally displays weak and broad bands at  $\sim 162\text{ cm}^{-1}$  ( $B_{1g}$  symmetry),  $\sim 538\text{ cm}^{-1}$  ( $E_g$  symmetry),  $\sim 667\text{ cm}^{-1}$  ( $A_{1g}$  symmetry), and  $\sim 750\text{ cm}^{-1}$  ( $B_{2g}$  symmetry). Here,  $A_{1g}$  and  $B_{2g}$  modes are assigned to mixed Mn–O stretching and Mn–O in-plane deformation, while the  $B_{1g}$  mode corresponds to out-of-plane bending vibrations [5]. References [5,53–55] report slightly different Raman spectra, which may be affected by sample degradation and spurious peaks. Nevertheless, the most intense  $A_{1g}$  band located at  $\sim 640\text{--}670\text{ cm}^{-1}$  is always present and can be used as a clear signature of  $\beta\text{-MnO}_2$  [5–7].

##### 3. Nsutite $\gamma\text{-MnO}_2$

Here,  $\gamma\text{-MnO}_2$  consists of a random intergrowth of  $\beta\text{-MnO}_2$  blocks within a matrix of orthorhombic ramsdellite  $\text{R-MnO}_2$  and exhibits a complex hexagonal tunneled structure with both  $(1 \times 1)$  and  $(1 \times 2)$  tunnels [7,56]. The Raman spectrum of  $\gamma\text{-MnO}_2$  is a combination of the spectra of  $\beta\text{-MnO}_2$  and  $\text{R-MnO}_2$  (not discussed here), and it depends on the fraction of pyrolusite within the ramsdellite matrix. Typically, it features a couple of peaks at  $\sim 572\text{--}582$  and  $\sim 654\text{--}658\text{ cm}^{-1}$  [7,53–55]. A detailed investigation into the Raman spectrum of  $\gamma\text{-MnO}_2$  can be found in Ref. [56].

##### 4. Birnessite $\delta\text{-MnO}_2$

Here,  $\delta\text{-MnO}_2$  is a layered  $\text{MnO}_2$  polymorph consisting of stacked layers of edge-sharing  $[\text{Mn}^{4+}\text{O}_6]$  octahedra [57]. When the predominant Mn oxidation state is  $+4$ , birnessite exhibits trigonal symmetry (space group  $R\bar{3}m$ ) [10]; however, especially in chemically synthesized and naturally occurring  $\delta\text{-MnO}_2$ , the presence of cations ( $\text{Na}^+, \text{K}^+, \text{Ca}^{2+}, \text{Mg}^{2+}$ , etc.) and/or water molecules in the interlayer spacing and the resulting decrease in the valence state of neighboring Mn cations reduce the overall crystal symmetry, leading to monoclinic (space group  $C2/m$ ) [7,10,57] or triclinic (space group  $P\bar{1}$ ) [6,10]  $\delta\text{-MnO}_2$ . In addition, in Ref. [10], it is claimed that, in recent years, the term  $\delta\text{-MnO}_2$  has been used to identify a variety of natural and synthetic phases—this may explain the

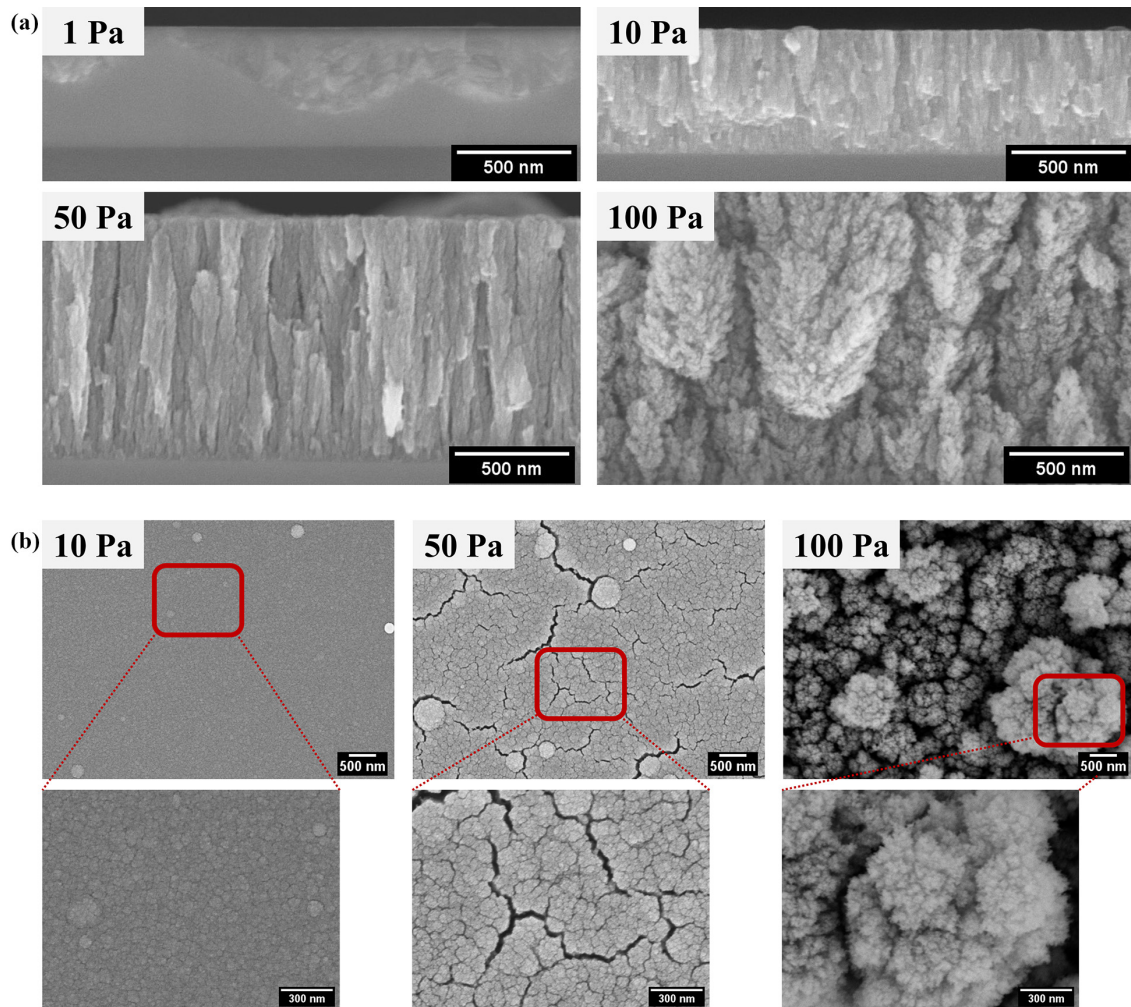


FIG. 1. (a) Scanning electron microscopy (SEM) cross-sectional images of the MnO<sub>x</sub> thin films deposited at 1, 10, 50, and 100 Pa of O<sub>2</sub> at constant laser fluence of  $\sim 2 \text{ J cm}^{-2}$  and 20 min deposition time. (b) Corresponding SEM top-view images and high magnifications of the films deposited at 10, 50, and 100 Pa of O<sub>2</sub>.

discrepancies across the Raman spectra of  $\delta\text{-MnO}_2$  from different references. In general, the Raman spectrum of  $\delta\text{-MnO}_2$  comprises three broad bands at  $\sim 504\text{--}509$ ,  $\sim 565\text{--}577$ , and  $635\text{--}646 \text{ cm}^{-1}$  [5,7,55,57], which could be assigned to Mn–O stretching vibrations in the  $[\text{Mn}^{4+}\text{O}_6]$  octahedra and in the basal plane of  $[\text{Mn}^{4+}\text{O}_6]$  sheets [57].

#### IV. RESULTS AND DISCUSSION

##### A. Morphology and structure of as-deposited MnO<sub>x</sub> films

Cross-sectional and top-view SEM images of as-deposited MnO<sub>x</sub> thin films are reported in Figs. 1(a) and 1(b), respectively. The presence of a background gas during the deposition strongly affects the film growth, and different film morphologies can be obtained by varying the O<sub>2</sub> pressure. Indeed, when the ablation plume produced after the laser-target interaction expands in vacuum or in a low-pressure atmosphere, the ablated species do not undergo collisions and reach the substrate with high kinetic energy, thus leading to a compact and smooth film. On the other hand, during ablation in high gas pressure, the plasma plume is confined by the gas, ablated

species lose kinetic energy due to multiple collisions, clusters start nucleating already in the gas phase, and the resulting film is porous and cluster assembled [71]. The MnO<sub>x</sub> film deposited at 1 Pa of O<sub>2</sub> is compact and smooth, while a columnar structure appears at 10 Pa and becomes more porous and less vertically aligned at 50 Pa. In the film deposited at 100 Pa, columns are replaced by treelike hierarchical assemblies, which are typical of metal oxides and nitrides produced by PLD in medium-high gas pressures [39,72–75]. Comparable morphology evolution is reported also in Ref. [27] for MnO<sub>2</sub> films grown by PLD in O<sub>2</sub> atmosphere from a metallic Mn target. As expected with PLD [39], the film thickness, with a fixed deposition time of 20 min, increases with increasing O<sub>2</sub> deposition pressure [Fig. 1(a)]. The corresponding deposition rates are estimated to be 25, 28, 53, and 98 nm min<sup>-1</sup> at 1, 10, 50, and 100 Pa of O<sub>2</sub>, respectively. In the top-view images of Fig. 1(b), the evolution of the surface morphology and porosity can be appreciated as well. The films grown at 10 and 50 Pa are characterized by cauliflowerlike features, corresponding to the apical parts of the columnar structures observed in the cross-sections of Fig. 1(a), whose size increases with

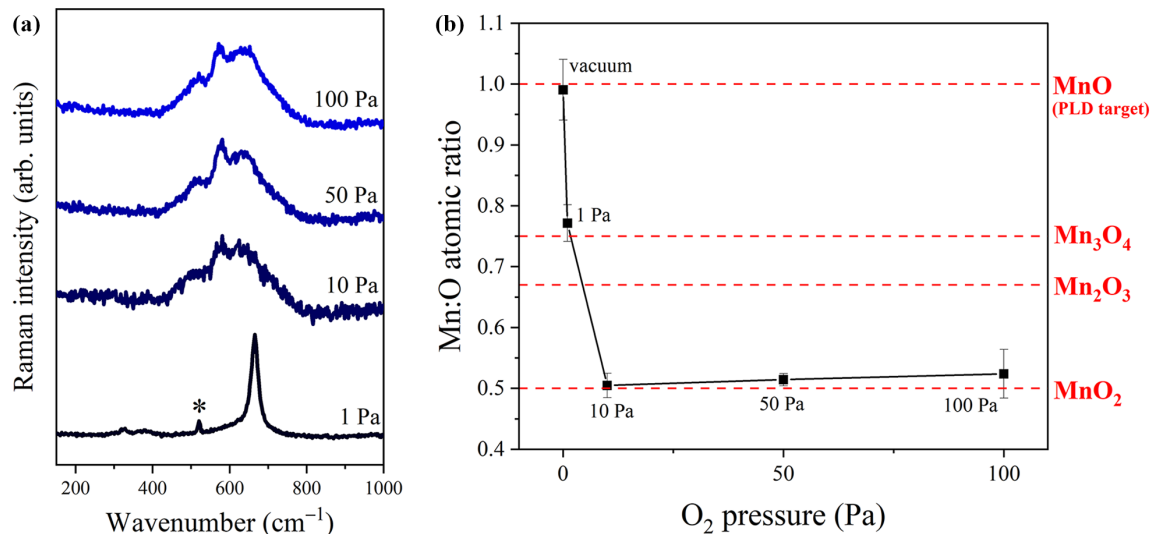


FIG. 2. (a) Raman spectra of as-deposited  $\text{MnO}_x$  films acquired using the 532 nm laser, 0.70 mW on the sample (\* indicates the  $520.7 \text{ cm}^{-1}$  Raman peak of the Si substrate). All spectra are reported after normalization. (b) Mn : O atomic ratio as estimated from energy-dispersive x-ray spectroscopy (EDXS) analysis of as-deposited  $\text{MnO}_x$  samples as a function of the  $\text{O}_2$  deposition pressure. All ratios are normalized to the value of 1.05 measured on stoichiometric MnO target. Red dashed lines indicate the nominal Mn : O ratio for four stoichiometric Mn oxide phases.

increasing  $\text{O}_2$  pressure. In addition, some branched cracks can be observed in the film deposited at 50 Pa. Finally, in the film grown at 100 Pa, the cauliflowerlike structures transform into highly porous clustered assemblies, and the overall morphology is more open.

The Raman spectra of as-deposited  $\text{MnO}_x$  films are reported in Fig. 2(a). Interestingly, the Raman spectrum of the film produced at 1 Pa of  $\text{O}_2$  is different from all the others and displays a sharp and intense peak at  $665 \text{ cm}^{-1}$  and two weak peaks at  $324$  and  $379 \text{ cm}^{-1}$ , which are close to the Raman bands reported for tetragonal hausmannite  $\text{Mn}_3\text{O}_4$  (see Sec. III B) [5–7,9]. The presence of narrow peaks and the good signal-to-noise ratio suggest a crystalline nature of this sample. On the other hand, the Raman spectra of  $\text{MnO}_x$  films deposited at 10, 50, and 100 Pa of  $\text{O}_2$  are similar, and all show a broad and structured band between 450 and  $800 \text{ cm}^{-1}$ , which can be deconvoluted into three main features at  $\sim 502$ ,  $573$ , and  $636 \text{ cm}^{-1}$ . These bands are well matched with those reported by Xin *et al.* [7] and Julien *et al.* [57] for monoclinic  $\delta$ - $\text{MnO}_2$ ; however, the assignment to a specific  $\text{MnO}_2$  polymorph is not straightforward due to the presence of large bands (see also Sec. III D 4), and we regard the as-deposited  $\text{MnO}_x$  films at 10, 50, and 100 Pa of  $\text{O}_2$  as amorphous/semicrystalline  $\text{MnO}_2$  (A- $\text{MnO}_2$ ). Further details about the structural properties of the as-deposited films will be provided in Sec. IV D, where XRD data are discussed. Since  $\text{MnO}_x$ -based materials are reported to suffer from degradation under the Raman laser beam [5,6], the reliability of Raman results was carefully assessed for any  $\text{MnO}_x$  phase and morphology in our acquisition conditions. The incident power on the sample of the 532 nm laser beam was gradually increased from 0.70 to  $> 8 \text{ mW}$ , until either clear spectral modifications or sample darkening in the optical image were detected. Especially on amorphous and porous films (see Fig. S2(b) in the Supplemental Material [44]),

significant spectral variations were observed at high incident powers, revealing the formation of a new phase with a strong peak at  $\sim 630$ – $640 \text{ cm}^{-1}$ . Such modifications were reported also by Bernardini *et al.* [6,76] and Post *et al.* [9] for  $\beta$ - $\text{MnO}_2$ , R- $\text{MnO}_2$ , and MnO and were ascribed to the laser-induced formation of a metastable spinellike phase [9]. Photoinduced damage, however, was observed on some samples well before any spectral change was detected (see, e.g., the sequence of optical images of Fig. S3 in the Supplemental Material [44], where a dark stain appears in the probed region already at 3.50 mW); therefore,  $\text{MnO}_x$  thin films on silicon can be effectively and safely characterized by Raman spectroscopy with the 532 nm excitation radiation—and with the acquisition parameters described in Sec. II B in terms of setup and measurement time—if the incident laser power is kept  $< 3 \text{ mW}$ . In this paper, unless otherwise specified, all Raman spectra were acquired using 0.70 mW incident power.

EDXS was employed to evaluate the elemental content of as-deposited  $\text{MnO}_x$  films and to further validate the phase assignment. Although EDXS suffers from low accuracy in the quantification of light elements, resulting in uncertainties in the absolute values, especially in the absence of calibration samples, it can still be a valuable technique to provide general trends about the dependency of the average atomic ratios on the  $\text{O}_2$  deposition pressure. Furthermore, measurement reliability was enhanced by assessing the Mn : O ratio of the pristine, not-ablated MnO target, which should be stoichiometric (i.e., Mn : O ratio equal to 1). Since the measured Mn : O ratio for the target is 1.05, all values reported in the following for  $\text{MnO}_x$  samples have been normalized to 1.05. In Fig. 2(b), the Mn : O atomic ratio of the films is plotted as a function of the  $\text{O}_2$  deposition pressure, along with the nominal ratios for stoichiometric MnO,  $\text{Mn}_3\text{O}_4$ ,  $\text{Mn}_2\text{O}_3$ , and  $\text{MnO}_2$ . The average atomic ratio for the  $\text{MnO}_x$  sample deposited at 1 Pa of  $\text{O}_2$  is 0.77, which is higher than the other samples

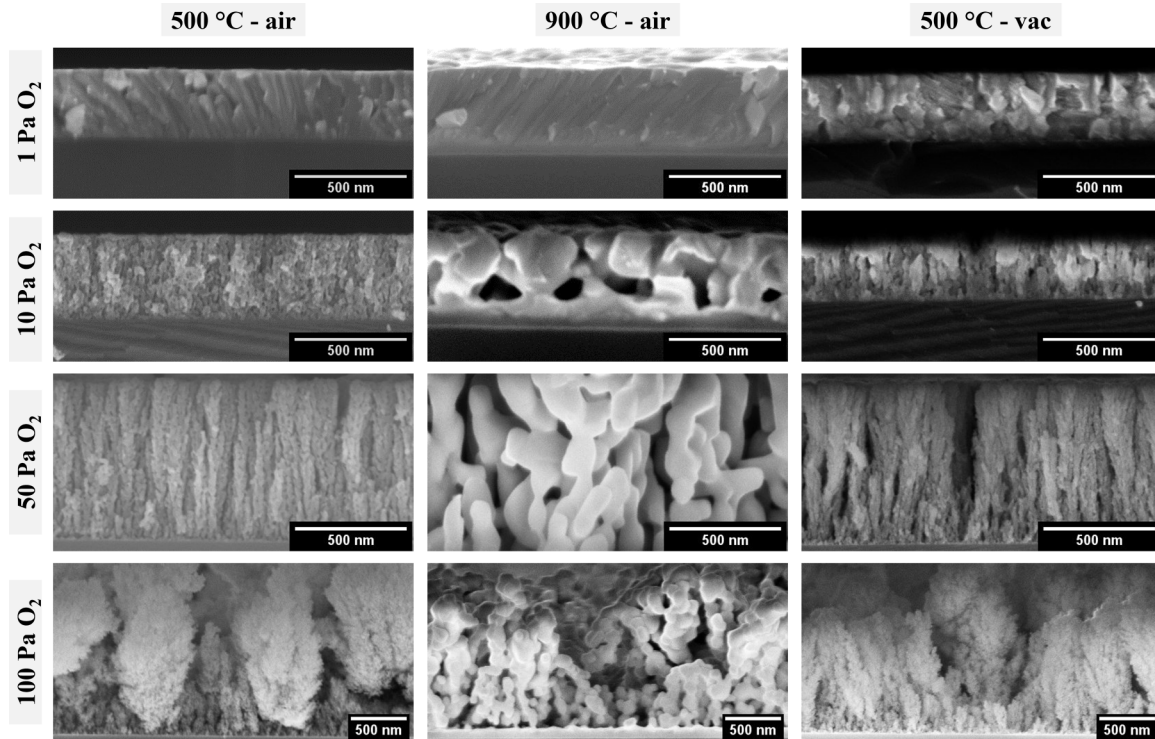


FIG. 3. Scanning electron microscopy (SEM) cross-sectional images of  $\text{MnO}_x$  thin films produced by pulsed laser deposition (PLD) at 1, 10, 50, and 100 Pa of  $\text{O}_2$ , after thermal annealing in different conditions. Based on the results of Raman spectroscopy, all samples annealed in air at both 500 and 900 °C correspond to the  $\alpha$ - $\text{Mn}_2\text{O}_3$  phase, while the samples annealed in vacuum at 500 °C consist of  $\text{Mn}_3\text{O}_4$ .

and closer to the nominal ratio for  $\text{Mn}_3\text{O}_4$ . Conversely, the average atomic ratios for  $\text{MnO}_x$  films grown at 10, 50, and 100 Pa of  $\text{O}_2$  are 0.50, 0.51, and 0.52, respectively, which agree with  $\text{MnO}_2$ . EDXS analysis confirms the phase diversity for the sample deposited at 1 Pa of  $\text{O}_2$ . As a result, room-temperature deposition in low  $\text{O}_2$  pressure from a  $\text{MnO}$  target leads to a less oxidized film containing low-valence Mn species, i.e.,  $\text{Mn}^{2+}/\text{Mn}^{3+}$  ( $\text{Mn}_3\text{O}_4$ ), rather than  $\text{Mn}^{4+}$  ( $\text{MnO}_2$ ). Finally, the average Mn : O atomic ratio for a sample deposited in vacuum ( $4 \times 10^{-3}$  Pa,  $\sim 1.7 \text{ J cm}^{-2}$ , 10 min deposition time; see Fig. S4 in the Supplemental Material for morphology [44]) is also reported in Fig. 2(b), being equal to 0.99. This value is  $\sim 1$ , i.e., close to the Mn : O ratio for stoichiometric  $\text{MnO}$ , indicating that ablation in the absence of  $\text{O}_2$  gas results in a poorly oxidized film whose composition matches the one of the target (therefore containing mostly  $\text{Mn}^{2+}$  species). To sum up, room-temperature PLD of a  $\text{MnO}$  target in the oxygen pressure range between vacuum and 100 Pa leads to  $\text{MnO}_x$  phases spanning  $\text{Mn}^{2+}$ ,  $\text{Mn}^{3+}$ , and  $\text{Mn}^{4+}$  oxidation states, corresponding to  $\text{MnO}$ ,  $\text{Mn}_3\text{O}_4$ , and  $\text{MnO}_2$  stoichiometries.

### B. Morphology and structure tuning by postdeposition annealing

To explore different regions of the Mn–O solid-state phase diagram [77] and to promote the film crystallization or transition to different oxide phases, as-deposited  $\text{MnO}_x$  films were subjected to thermal annealing at 500 and 900 °C in air and 500 °C in vacuum. SEM cross-sectional images of annealed  $\text{MnO}_x$  films in different annealing conditions are reported in

Fig. 3. The postdeposition thermal treatment induces morphological changes and sintering effects in all films. For  $\text{MnO}_x$  films grown at 1 Pa of  $\text{O}_2$ , the compact structure of the as-deposited material is maintained; however, oblique columnar grains are visible after annealing in air at both 500 and 900 °C. A more disordered structure comprising irregular-shaped grains and some voids is obtained after annealing in vacuum at 500 °C. In the case of the  $\text{MnO}_x$  films deposited at 10 and 50 Pa of  $\text{O}_2$ , air annealing at 500 °C results in a variation of the nanoscale porosity and an enlargement of the grains constituting the vertical features of the film, even if the overall columnar morphology is preserved, especially for the film produced at 50 Pa of  $\text{O}_2$ . A similar effect is noticed also after annealing in vacuum: in the film deposited at 10 Pa of  $\text{O}_2$ , columns are replaced by vertically aligned jagged grains and more voids are visible, while in the film deposited at 50 Pa of  $\text{O}_2$ , the porous columns are well distinguishable but more far apart. On the contrary, severe coalescence within the columns occurs at 900 °C, leading to a film constituted by an arrangement of substantially larger, dense, and interconnected structures separated by cavities. Finally, for  $\text{MnO}_x$  films deposited at 100 Pa of  $\text{O}_2$ , the thermal treatment does not significantly alter the porous structure of the treelike assemblies both in air and in vacuum at 500 °C. Instead, an obvious modification is observed after air annealing at 900 °C, which causes a strong coalescence, the complete loss of the porous assemblies, and the formation of a network of dense and tangled filaments, comparable with those obtained in the film deposited at 50 Pa of  $\text{O}_2$ .

The SEM top-view images of Fig. 4 confirm the morphological and structural changes occurred in  $\text{MnO}_x$  films after



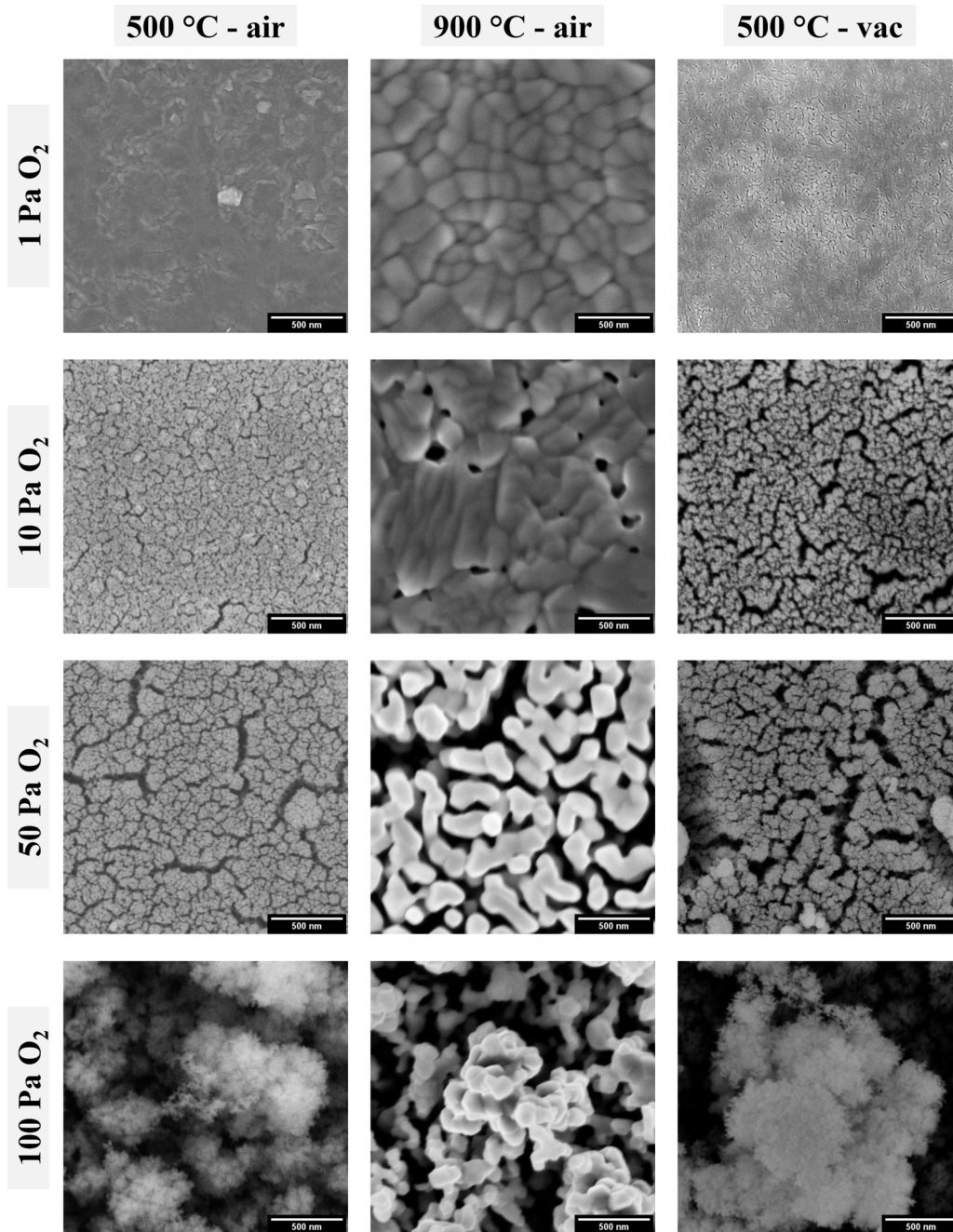


FIG. 4. Scanning electron microscopy (SEM) top-view images of  $MnO_x$  thin films produced by pulsed laser deposition (PLD) at 1, 10, 50, and 100 Pa of  $O_2$ , after thermal annealing in different conditions.

different annealing treatments. Annealing in air at  $500\text{ }^\circ\text{C}$  does not significantly alter the general film morphology [see Fig. 1(b) for comparison with as-deposited top-view images], while a massive coalescence resulting in large and regular crystalline grains occurs at  $900\text{ }^\circ\text{C}$ . Moreover, in the central column of Fig. 4, it can be noticed how the degree of voids increases with increasing  $O_2$  deposition pressure: indeed, isolated holes start forming across grains at 10 Pa, and then an interconnected network of voids appears at 50 Pa and expands at 100 Pa. The surface morphology of films annealed in vacuum at  $500\text{ }^\circ\text{C}$  is like the one observed at the same annealing temperature in air; however, a more significant surface cracking is noticed at any  $O_2$  pressure.

Like as-deposited  $MnO_x$  films, annealed films were characterized by Raman spectroscopy to disclose any phase transition and crystallization process. The Raman spectra of the  $MnO_x$  film grown at 1 Pa of  $O_2$  after thermal annealing are reported in Fig. 5(a), along with the spectrum of the as-deposited film. Vacuum annealing at  $500\text{ }^\circ\text{C}$  maintains the  $Mn_3O_4$  phase; however, all the main peaks—here labeled Peak H1, H2, and H3—are more defined and redshifted compared to the as-deposited film: indeed, Peak H1 shifts from  $324$  to  $\sim 321\text{ cm}^{-1}$ , Peak H2 from  $379$  to  $\sim 374\text{ cm}^{-1}$ , and Peak H3 from  $665$  to  $660\text{ cm}^{-1}$  [see Figs. 6(a) and 6(b) and Table II(a)]. The peak positions of the vacuum-annealed film perfectly match with those of bulk crystalline hausmannite

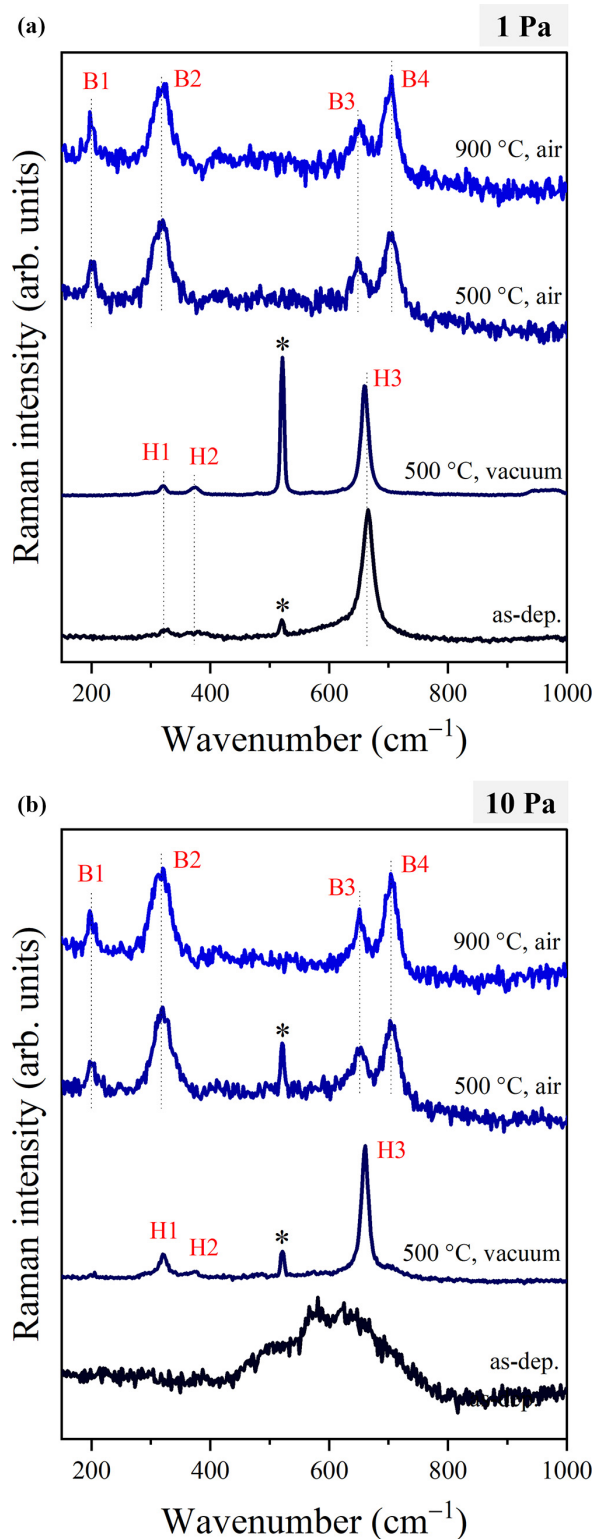


FIG. 5. Raman spectra of  $\text{MnO}_x$  films deposited at (a) 1 Pa and (b) 10 Pa of  $\text{O}_2$ , before and after thermal annealing in different conditions (\* indicates the  $520.7 \text{ cm}^{-1}$  Raman peak of the Si substrate). For both values of  $\text{O}_2$  pressure, also the Raman spectrum of the as-deposited film is reported. All spectra are reported after normalization.

TABLE II. Position and width (expressed as FWHM) of the main Raman peaks of hausmannite  $\text{Mn}_3\text{O}_4$  in (a) the as-deposited and vacuum-annealed film grown by PLD at 1 Pa of  $\text{O}_2$ , and (b) the vacuum-annealed film grown by PLD at 10 Pa of  $\text{O}_2$ .

Peak	As-deposited		500 °C, vacuum	
	Position ( $\text{cm}^{-1}$ )	FWHM ( $\text{cm}^{-1}$ )	Position ( $\text{cm}^{-1}$ )	FWHM ( $\text{cm}^{-1}$ )
(a) 1 Pa $\text{O}_2$				
H1	324	27.2	321	12.2
H2	379	48.2	374	18.5
H3	665	22.6	660	14.1
(b) 10 Pa $\text{O}_2$				
H1			321	16.2
H2			372	14.1
H3			660	14

[50] (see also Sec. III B), indicating a better crystallization into the spinel phase with respect to the as-deposited film. In addition, improved crystalline quality is highlighted by a decrease of the width—expressed as FWHM of the fitting Lorentzian functions—for the three peaks [Fig. 6(c) and Table II(a)]. Further details will be added in Sec. IV D. Interestingly, the enhanced intensity of the Si peak at  $520.7 \text{ cm}^{-1}$  suggests higher film transparency to the laser beam after vacuum annealing, in line with changes in the optical properties of films deposited on a transparent substrate (see Fig. S5 in the Supplemental Material [44]). Such variations could be the result of a combined effect of morphology and absorption properties of the film. Figure 6 also reports the  $\text{Mn}_3\text{O}_4$  peak positions and widths for the 1 Pa film annealed in air at  $300 \text{ °C}$  for 4 h: This annealing condition does not promote any phase transition; however, it improves the crystalline quality of the film, and the resulting spectrum is intermediate between the as-deposited and the vacuum-annealed ones. Indeed, phase transformation upon annealing in air occurs starting from  $500 \text{ °C}$ , as inferred from the Raman spectrum reported in Fig. 5(a), and a similar result is achieved up to  $900 \text{ °C}$ . The Raman spectra acquired after air annealing at both 500 and  $900 \text{ °C}$  feature four main peaks—here labeled B1, B2, B3, and B4—which agree with those reported in Refs. [7,9] for bixbyite  $\alpha\text{-Mn}_2\text{O}_3$  despite slight differences in the relative intensity ratios (see also Sec. III C). Details about the peak parameters can be found in Table III(a), even if no clear trends as a function of the  $\text{O}_2$  deposition pressure or the annealing temperature can be observed (see also Fig. S6 in the Supplemental Material [44]).

Figure 5(b) compares the Raman spectra of as-deposited and annealed  $\text{MnO}_x$  films grown at 10 Pa of  $\text{O}_2$ . The starting material was identified by Raman and EDXS analysis as amorphous  $\text{MnO}_2$  (see Sec. IV A); in the same way as in the case of 1 Pa, phase transition to hausmannite  $\text{Mn}_3\text{O}_4$  and to bixbyite  $\alpha\text{-Mn}_2\text{O}_3$  can be recognized after annealing in vacuum at  $500 \text{ °C}$  and in air at both 500 and  $900 \text{ °C}$ , respectively. Slight variations in the positions, widths, and relative intensity ratios of the peaks can be appreciated, as reported in Fig. S6 in the Supplemental Material [44] and in Tables II(b) and III(b). As far as the samples deposited at 50 and 100 Pa of  $\text{O}_2$  are

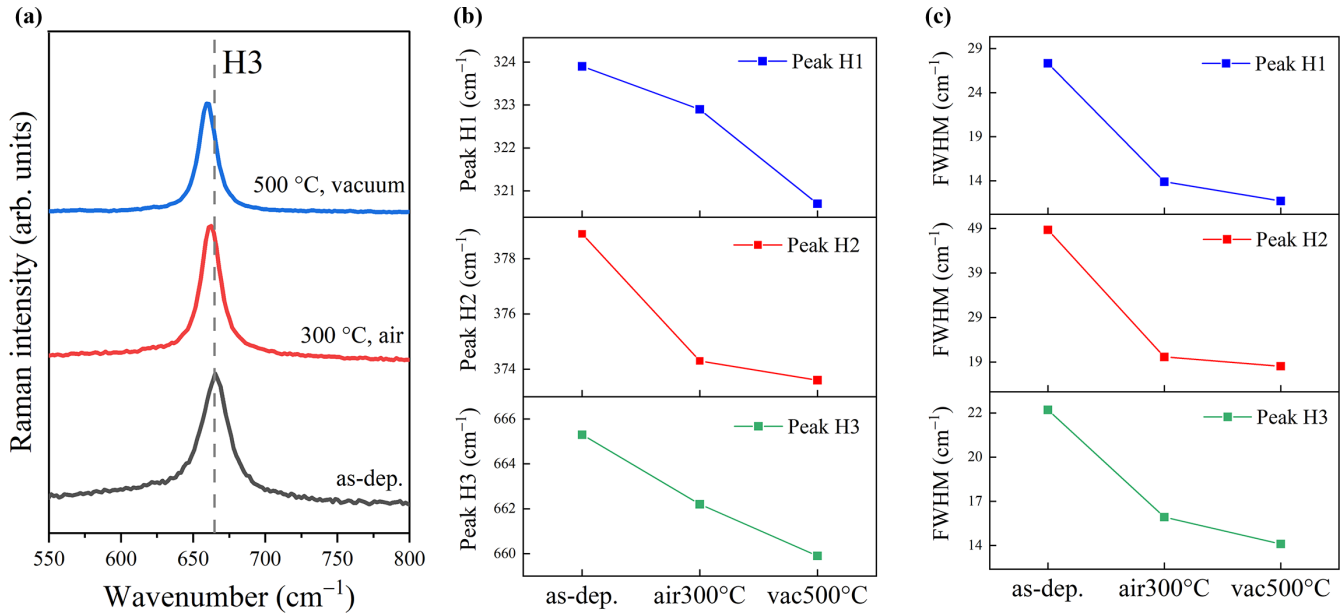


FIG. 6. (a) Raman spectra of  $\text{MnO}_x$  films deposited at 1 Pa of  $\text{O}_2$  in the spectral region 550–800  $\text{cm}^{-1}$  (centered around the main  $A_{1g}$  peak of  $\text{Mn}_3\text{O}_4$ , herein labeled as Peak H3). Trends of (b) the position and (c) the width [expressed as full width at half-maximum (FWHM)] of Peaks H1, H2, and H3 of as-deposited and annealed films grown at 1 Pa of  $\text{O}_2$ .

concerned, the phase evolution upon air annealing is comparable with that at 10 Pa (see Figs. S6 and S7 and Table SII in the Supplemental Material [44]), with formation of  $\alpha\text{-Mn}_2\text{O}_3$  at both 500 and 900 °C. On the other hand, the Raman spectra after vacuum annealing at 500 °C reveal not only the main H3 peak of hausmannite at  $\sim 659 \text{ cm}^{-1}$  but also a broad band extending down to  $\sim 500 \text{ cm}^{-1}$  and the strong signature of the silicon substrate at  $520.7 \text{ cm}^{-1}$  (Fig. S8 in the Supplemental Material [44]), while peaks H1 and H2 are hardly detectable in both samples. The spectral shape, along with the broadening of H3 compared with the 1 and 10 Pa cases (see Table SIII in the Supplemental Material [44]), suggests an incomplete crystallization of the films caused by their enhanced porosity, resulting in  $\text{Mn}_3\text{O}_4$  nanocrystals embedded in an amorphous

$\text{MnO}_x$  matrix [78]. To qualitatively identify a temperature threshold for phase transformation both in vacuum and in air, supplementary annealing treatments were carried out on selected samples: Air annealing at 300, 400, and 450 °C does not alter the amorphous nature of as-deposited samples [the structured Raman band observed in Fig. 2(a) tends to be replaced by a broader and less-defined band, probably indicating further amorphization], while transition to  $\alpha\text{-Mn}_2\text{O}_3$  occurs in the range 500–900 °C. On the other hand, annealing in vacuum leads to  $\text{Mn}_3\text{O}_4$  phase already at 400 °C. It is worth mentioning that the previous evaluations do not hold for samples deposited in vacuum, i.e., for MnO films; in this case, annealing in air at 400 °C leads to phase transition to hausmannite  $\text{Mn}_3\text{O}_4$ .

TABLE III. Position and width (expressed as FWHM) of the main Raman peaks of bixbyite  $\alpha\text{-Mn}_2\text{O}_3$  in the films grown by PLD at (a) 1 and (b) 10 Pa of  $\text{O}_2$  and annealed in air at 500 and 900 °C.

Peak	500 °C, air		900 °C, air	
	Position ( $\text{cm}^{-1}$ )	FWHM ( $\text{cm}^{-1}$ )	Position ( $\text{cm}^{-1}$ )	FWHM ( $\text{cm}^{-1}$ )
(a) 1 Pa $\text{O}_2$				
B1	202	13.1	200	18.8
B2	317	39.9	318	35.6
B3	649	25.4	651	25.3
B4	704.5	29	702	26.5
(b) 10 Pa $\text{O}_2$				
B1	201	19.1	201	15.5
B2	319	38.7	318.5	38.2
B3	652.5	26.1	653	15.2
B4	704	26.7	703	28.2

Compositional EDXS analysis was performed also on annealed  $\text{MnO}_x$  films, employing the same normalization procedure discussed in Sec. IV A. The Mn:O atomic ratios for annealed films are plotted in Fig. 7, along with the nominal ratios for stoichiometric  $\text{Mn}_3\text{O}_4$ ,  $\text{Mn}_2\text{O}_3$ , and  $\text{MnO}_2$ . The Mn:O ratio for the as-deposited films is reported as well for comparison. It is worth noticing that the Mn:O atomic ratios for annealed samples deposited at 100 Pa of  $\text{O}_2$  are not reported since the EDXS data were highly dispersed and not consistent with the Raman phase assignment. This issue probably arose because of the increased porous nature of the samples and the significant hindrance of the signal coming from the silicon substrate.

Focusing on the 1–50 Pa  $\text{O}_2$  pressure range, the normalized Mn:O atomic ratios fall between 0.75 and 0.78 for all vacuum-annealed samples, in agreement with  $\text{Mn}_3\text{O}_4$  phase, whose nominal ratio is 0.75. Good agreement with the stoichiometric value of 0.67 ( $\text{Mn}_2\text{O}_3$ ) is also achieved for the samples annealed in air at 900 °C, whose Mn:O ratios are in the range 0.66–0.70. Surprisingly, larger deviations are observed when samples are annealed in air at 500 °C: Even

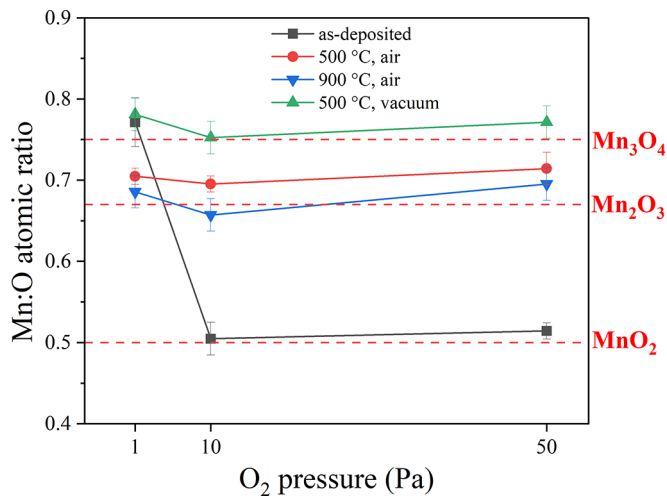


FIG. 7. Mn : O atomic ratio as estimated from energy-dispersive x-ray spectroscopy (EDXS) analysis of as-deposited and annealed  $\text{MnO}_x$  samples as a function of the  $\text{O}_2$  deposition pressure in the range 1–50 Pa. All ratios are normalized to the value of 1.05 measured on stoichiometric MnO target. Red dashed lines indicate the nominal Mn : O ratio for three stoichiometric Mn oxide phases.

if the same  $\text{Mn}_2\text{O}_3$  phase is expected according to Raman spectroscopy (see Fig. 5), the Mn : O ratios are slightly higher at  $\sim 0.70$ . Nonetheless, recalling the limitations of EDXS quantitative analysis—especially in the presence of low-Z elements like oxygen—the results of Fig. 7 are coherent with the Raman phase assignment.

### C. Chemical investigation by XPS of as-deposited and annealed films

EDXS results about the film composition and stoichiometry are complemented by XPS analysis, which can provide details on the chemical state of Mn cations. Figures 8(a) and 8(b) show the photoemission signal in the Mn  $2p$  and O  $1s$  BE regions acquired from three representative  $\text{MnO}_x$  films grown by PLD in a background pressure of (i) 10 Pa of  $\text{O}_2$ , either as-deposited (black dots) or after air annealing at 500 °C (red dots), and (ii) 1 Pa of  $\text{O}_2$  (blue dots).

Photoemission from Mn  $2p$  orbital results in two spin-orbit split peaks [the Mn  $2p_{3/2}$  and Mn  $2p_{1/2}$  features shown in Fig. 8(a)]. Each peak is characterized by a quite broad line shape, commonly attributed to the multiplet splitting of the main photoemission line [79,80]. The fine structure of the photoemission peaks cannot be resolved in our data; however, a clear shift toward lower BE is visible. The BE of the Mn  $2p_{3/2}$  feature, for instance, moves from  $\sim 642.0$  eV (black spectrum, as-deposited film at 10 Pa of  $\text{O}_2$ ) to  $\sim 641.3$  eV (blue spectrum, as-deposited film at 1 Pa of  $\text{O}_2$ ), compatible with a change in the oxidation state of the Mn cations from +4, as in  $\text{MnO}_2$ , to +3 or a mixture of +3/+2, as in  $\text{Mn}_2\text{O}_3$  or in the mixed-valence oxide  $\text{Mn}_3\text{O}_4$ , respectively [41,79–83]. The main O  $1s$  peak [Fig. 8(b)], attributed to lattice O, is located at about the same BE in all the samples, as expected from the nominal  $-2$  oxidation state of O anions. The shoulder at higher BE in Fig. 8(b) is attributed to the presence of surface hydroxyls or adsorbed water [82,83]. Further insight

into the Mn oxidation state in the analyzed films is obtained by looking at the characteristic multiplet splitting of the Mn  $3s$  line [Fig. 8(c)], resulting from the strong exchange interaction between the unpaired valence electrons and the  $3s$  core hole left upon photoemission [84]. In agreement with the analysis of the Mn  $2p_{3/2}$  feature, the measured BE differences between the two  $3s$  peaks show a monotonic evolution from 4.9 eV (as-deposited film at 10 Pa of  $\text{O}_2$ ) to 5.4 eV (air-annealed film) and 5.5 eV (as-deposited film at 1 Pa of  $\text{O}_2$ ). A correlation is established in the literature between the Mn  $3s$  splitting and the oxidation state of the Mn cations: A splitting in the 5.2–5.6 eV range is reported for photoemission from Mn +3 or a mixed +3/+2 ion population, while a value ranging from 4.5 to 4.7 eV is reported for Mn +4 cations [41,81,85].

The spectroscopic results from the air-annealed sample grown at 10 Pa of  $\text{O}_2$  and the as-deposited sample grown at 1 Pa of  $\text{O}_2$  are compatible with photoemission from either a  $\text{Mn}_2\text{O}_3$  or a  $\text{Mn}_3\text{O}_4$  oxide, with the experimental data suggesting a lower overall Mn oxidation state in the latter film. However, given the absence of clear satellite structures and/or a peculiar line shape characteristic of pure Mn +3 or Mn +2 phases (as also reported in the literature, see, e.g., Ref. [41]), it is rather difficult, based on XPS alone, to assess the exact stoichiometry of the two films. On the other hand, the spectra related to the as-deposited film grown at 10 Pa of  $\text{O}_2$  are compatible with the  $\text{MnO}_2$  stoichiometry retrieved from the previous analyses. We point out, however, the presence of broader line shapes with respect to the  $\text{MnO}_2$  spectra reported in the literature [41,82] and the spectra recorded from the other two samples, especially in the Mn  $3p$  region [Fig. 8(c)]. This difference, along with the slightly larger-than-expected Mn  $3s$  splitting, might be ascribed to a small contribution from reduced Mn species, present in the oxide matrix at least within the XPS information depth [86].

### D. Structural investigation by XRD of as-deposited and annealed films

XRD measurements carried out on selected  $\text{MnO}_x$  films mostly confirmed the results of Raman spectroscopy discussed in Secs. IV A and IV B. The x-ray powder diffraction patterns of six  $\text{MnO}_x$  phases are reported in Fig. S9 in the Supplemental Material [44] as a reference (derived either from the MINCRYST database [87] or from the American Mineralogist Crystal Structure Database [88]). The GIXRD patterns of the as-deposited and annealed films grown at 1 Pa of  $\text{O}_2$  are plotted in Fig. 9(a). The x-ray pattern of the as-deposited film [Fig. 9(a), green curve] is characterized by three main broad and asymmetric peaks at  $\sim 16.9^\circ$ ,  $\sim 27.6^\circ$ , and  $\sim 31.6^\circ$ , which correspond to the (101), (112), and (103) reflections of  $\text{Mn}_3\text{O}_4$  phase, as can be inferred by comparing it with the powder reference pattern of tetragonal spinel hausmannite [89]. The broadness of the peaks, their slight angular shift, and the poor signal-to-noise ratio of the XRD pattern suggest a distorted and nanocrystalline nature for this sample [90], while the peak asymmetry could be ascribed to poorly crystalline components along the same crystallographic directions. After vacuum-annealing at 500 °C for 1 h, the XRD peaks become sharper and closer to the powder reference values [Fig. 9(a), red curve], and new reflections

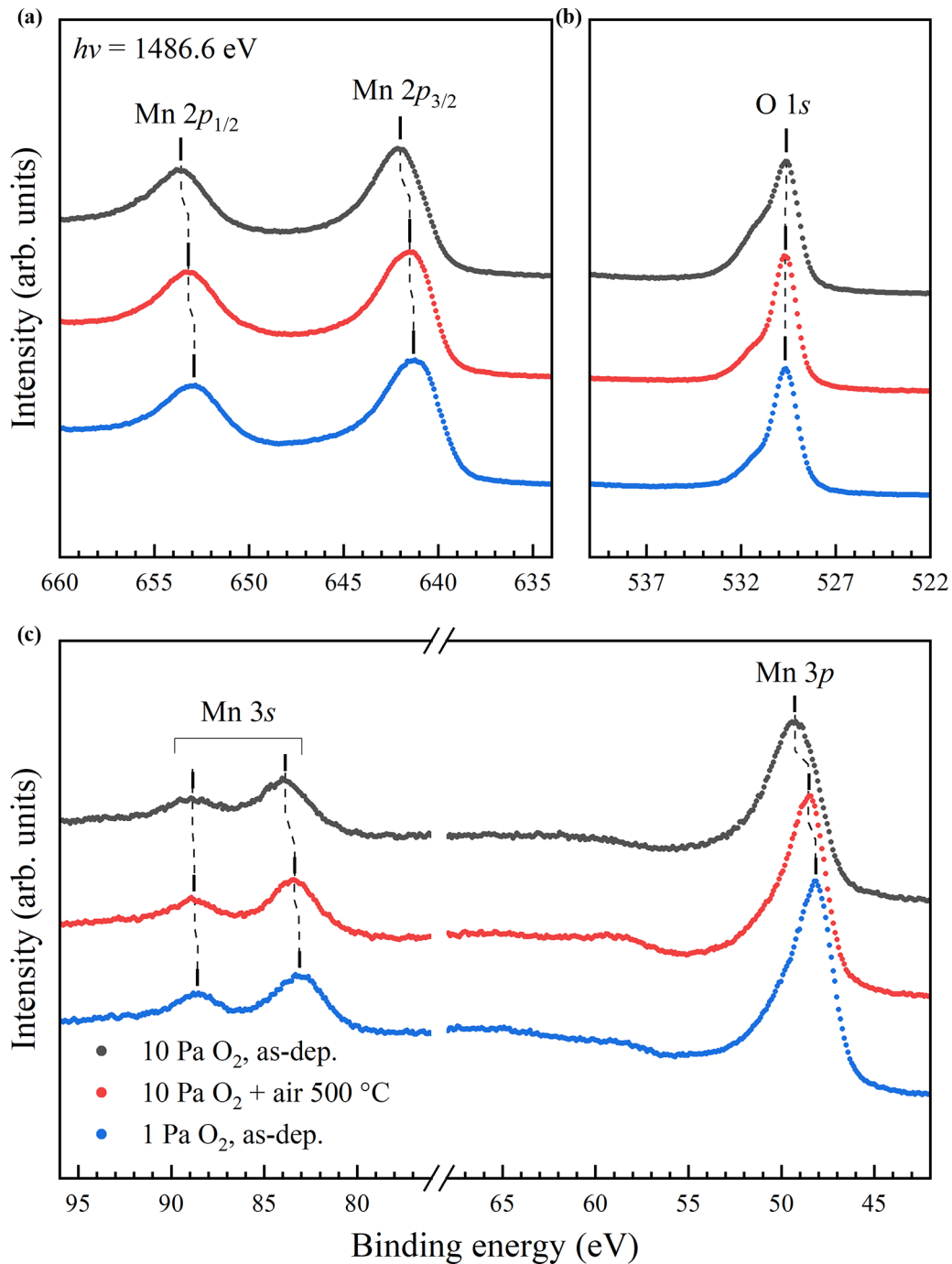


FIG. 8. X-ray photoelectron spectroscopy (XPS) (a) Mn 2p, (b) O 1s, and (c) Mn 3s and Mn 3p profiles from as-deposited (black dots) and air-annealed (red dots) MnO<sub>x</sub> thin films grown by pulsed laser deposition (PLD) at 10 Pa of O<sub>2</sub> and from an as-deposited (blue dots) MnO<sub>x</sub> thin film grown by PLD at 1 Pa of O<sub>2</sub>. For clarity, the three set of spectra have been vertically offset and normalized to (a) and (b) the peak Mn 2p<sub>3/2</sub> intensity and (c) the peak Mn 3s intensity.

are visible, i.e., (211), (105), and (224). The absence of some reflections and the differences in the relative intensity ratios compared with the reference pattern—see, e.g., the (101) vs (211) peaks—may indicate a preferential crystal orientation of the film along specific crystallographic directions. Quantitative analysis of the experimental GIXRD data was performed via Rietveld refinement on the angular range 10–70°, based on the powder reference pattern of tetrago-

nal Mn<sub>3</sub>O<sub>4</sub> (space group  $I4_1/amd$ , ICSD #68174 [91,92]) as the initial input (Fig. S10 in the Supplemental Material [44]). Single-crystalline phase was confirmed in both samples. Moreover, lattice parameters and average crystallite size (expressed as coherent crystal domains) were determined, as listed in Table IV. The as-deposited film is characterized not only by smaller crystal grains but also by larger lattice parameters and by a wider unit cell volume with respect to the

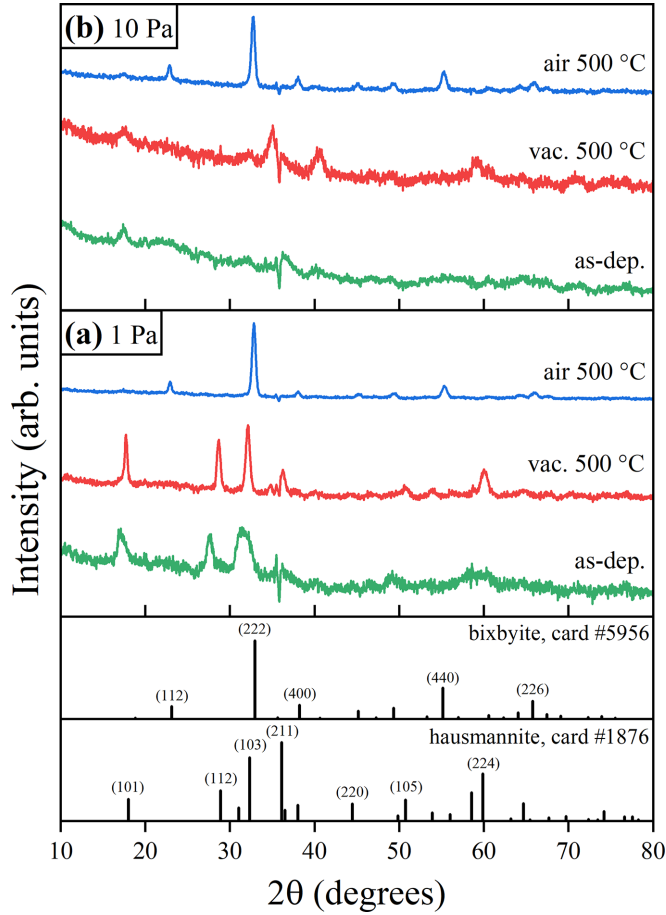


FIG. 9. Grazing incidence x-ray diffraction (GIXRD) patterns of as-deposited and annealed  $\text{MnO}_x$  thin films grown by pulsed laser deposition (PLD) at (a) 1 Pa and (b) 10 Pa of  $\text{O}_2$ . Experimental data are compared with the powder reference patterns of tetragonal hausmannite  $\text{Mn}_3\text{O}_4$  (MINCRYST database card #1876 [89]) and cubic bixbyite  $\alpha\text{-Mn}_2\text{O}_3$  (MINCRYST database card #5956 [94]).

bulk values [92], coherently with the observed peak shifts to lower angles in the corresponding GIXRD pattern of Fig. 9(a). After vacuum annealing at 500 °C, the unit cell shrinks, and the lattice constant  $a$  gets closer to that of bulk  $\text{Mn}_3\text{O}_4$ . This variation of lattice parameters is accompanied by an increase in the average grain size of about one order of magnitude, consistent with peak narrowing. These findings also justify the blueshift of the main Raman peaks of  $\text{Mn}_3\text{O}_4$  detected in the spectrum of the as-deposited sample [Figs. 6(a) and 6(b)], suggesting phonon confinement effects in the small grains ( $\sim 30$  nm), in accordance with Ref. [93]. After annealing in air at 500 °C [Fig. 9(a), blue curve], the GIXRD pattern

matches that of cubic bixbyite  $\alpha\text{-Mn}_2\text{O}_3$  [94], as expected from Raman analysis.

Considering samples deposited at 10 Pa of  $\text{O}_2$ , the GIXRD patterns of as-deposited and annealed films are reported in Fig. 9(b). No specific peaks are observed for the as-deposited film [Fig. 9(b), green curve]—except for a broad feature at  $\sim 17.4^\circ$  and a hump between  $35^\circ$  and  $40^\circ$ —which was assumed to be amorphous by Raman spectroscopy. In addition, the signal-to-noise ratio of the x-ray pattern is poor. After air annealing at 500 °C [Fig. 9(b), blue curve], sharp and narrow peaks appear at the angular positions of the powder reference pattern of bixbyite [94], implying the film crystallization to polycrystalline  $\alpha\text{-Mn}_2\text{O}_3$ . Interestingly, as in the case of 1 Pa of  $\text{O}_2$ , the relative intensity ratios match those of the reference x-ray pattern, suggesting no preferential crystal orientation in both cases. The GIXRD pattern of the vacuum-annealed sample [Fig. 9(b), red curve] is characterized by a noisy background and broad features at  $\sim 17.5^\circ$ ,  $\sim 32.3^\circ$ ,  $\sim 35.0^\circ$ , and  $\sim 59.1^\circ$ , which can be assigned to the (101), (103), (211), and (224) reflections of  $\text{Mn}_3\text{O}_4$ , respectively. The additional peak at  $\sim 40.6^\circ$  seems to correspond to none of  $\text{Mn}_3\text{O}_4$  reflections and could be related to minor traces of less oxidized cubic  $\text{MnO}$ , whose main (200) reflection is located at  $40.55^\circ$  [95] (see Fig. S9(a) in the Supplemental Material [44]). Interestingly, the GIXRD results indicate a poor long-range crystalline order for this sample in contrast to the well-defined Raman peaks of Fig. 5(b) revealing superior short-range atomic ordering. Finally, the GIXRD pattern of the sample grown in vacuum, i.e.,  $4 \times 10^{-3}$  Pa (Fig. S11 in the Supplemental Material [44]), has a poor signal-to-noise ratio and shows peaks corresponding to the (111), (200), and (113) reflections of cubic manganosite  $\text{MnO}$  [95].

The phase stability regions for  $\text{MnO}_x$  thin films as a function of  $\text{O}_2$  deposition pressure and annealing temperature are tentatively reported in Fig. 10(a) (air annealing) and Fig. 10(b) (vacuum annealing), cross-validated by multiple characterization techniques including Raman, EDXS, XPS, and XRD. The boundaries between the phases are qualitative, and additional extensive measurements involving other PLD and annealing conditions are necessary for a complete picture.

#### E. The role of the substrate: The case of $\text{Na}^+$ ions

The morphological and phase characterization presented in Secs. IV A–IV D was limited exclusively to  $\text{MnO}_x$  thin films deposited on Si substrates (except for films grown on Pt-coated Si or Ti foil aimed at XPS analysis, for which no Raman or SEM variations were detected with respect to bare Si). The type of substrate is known to affect the film growth in terms of crystal orientation and surface mobility

TABLE IV. Lattice parameters and crystallite domain size (expressed as coherent crystal domain) derived from Rietveld refinement of GIXRD experimental data. The crystal data of bulk hausmannite  $\text{Mn}_3\text{O}_4$  are also reported.

Sample	$a = b$ (Å)	$c$ (Å)	$ca$	Cell volume ( $\text{nm}^3$ )	Domain size (nm)
1 Pa $\text{O}_2$ , as-deposited	$5.852 \pm 0.014$	$9.451 \pm 0.014$	1.62	$0.3240 \pm 0.0020$	$30.01 \pm 6.87$
1 Pa $\text{O}_2$ , vacuum, 500 °C	$5.701 \pm 0.002$	$9.415 \pm 0.003$	1.65	$0.3060 \pm 0.0003$	$187.28 \pm 118.46$
$\text{Mn}_3\text{O}_4$ bulk [92]	5.765	9.442	1.64	0.3143	–

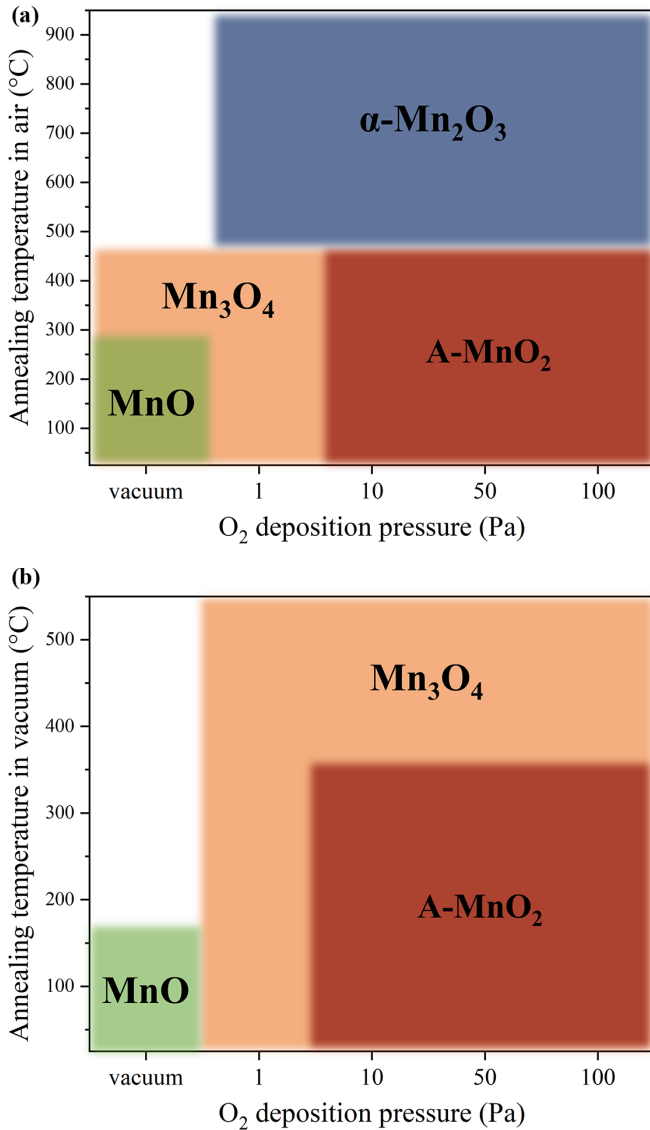


FIG. 10. Qualitative stability regions for different  $MnO_x$  phases obtained on Si substrates by several combinations of  $O_2$  deposition pressure and annealing temperature in (a) air and (b) vacuum. The blank regions have not been explored in this paper.

of ablated species [22,71]; however, it should not alter the  $MnO_x$  phase [23]. Depositions of  $MnO_x$  films on soda-lime and FTO-coated glass slides and postdeposition thermal annealing in selected conditions were therefore carried out to check the phase reproducibility on different substrates. No significant differences were detected by Raman spectroscopy for as-deposited and annealed  $MnO_x$  films on FTO-coated glass (Fig. S12(a) in the Supplemental Material [44]) and for as-deposited  $MnO_x$  films on soda-lime glass (Fig. S12(b) in the Supplemental Material [44]). On the contrary, air annealing at 500 °C, 2 h, of  $MnO_x$  films grown on soda-lime glass did not lead to bixbyite  $\alpha-Mn_2O_3$ , as in the case of Si substrates, but to hollandite  $\alpha-MnO_2$ . Indeed, the corresponding Raman spectrum of Fig. 11(a) is markedly different from that of  $\alpha-Mn_2O_3$ , and it is characterized by four intense and sharp peaks at 184, 392, 580, and 644  $cm^{-1}$ , well-matched with those previously published for  $\alpha-MnO_2$  [7,52]. The formation

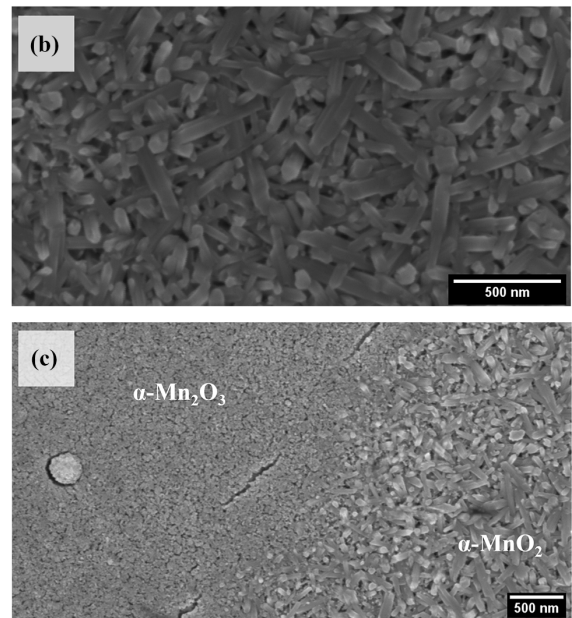
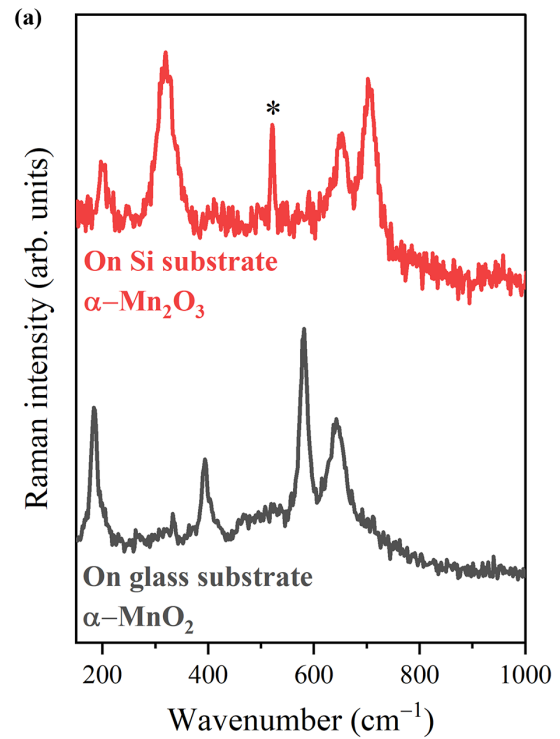


FIG. 11. (a) Raman spectra of  $MnO_x$  films deposited at 10 Pa of  $O_2$  and annealed in air at 500 °C, 2 h, on a Si substrate (red curve) and on a soda-lime glass substrate (gray curve). The spectra are reported after normalization (\* indicates the 520.7  $cm^{-1}$  Raman peak of the Si substrate). (b) Scanning electron microscopy (SEM) top-view image of Na-stabilized  $\alpha-MnO_2$  nanorods obtained during air annealing at 500 °C, 2h, of a  $MnO_x$  film grown at 10 Pa of  $O_2$  on a Si substrate, in the presence of  $Na_2SO_4$  aqueous solution. (c) SEM top-view image of the boundary region between  $\alpha-Mn_2O_3$  and Na-stabilized  $\alpha-MnO_2$  nanorods.

of  $\alpha-MnO_2$  is expected to result from the thermally activated solid-state interdiffusion of  $Na^+$  and/or  $K^+$  ions present in the soda-lime glass, which contains 13.0% of  $Na_2O$  and 0.3% of

$\text{K}_2\text{O}$  [96]. As reported in Sec. III D 1, the tunneled ( $2 \times 2$ ) structure of hollandite  $\alpha\text{-MnO}_2$  is typically stabilized by metallic cations, including  $\text{Na}^+$  and  $\text{K}^+$  [52]. The film crystallization to  $\alpha\text{-MnO}_2$  was confirmed also by GIXRD (Fig. S13 in the Supplemental Material [44]), which highlighted the coexistence of both bixbyite  $\alpha\text{-Mn}_2\text{O}_3$  and hollandite  $\alpha\text{-MnO}_2$ , the latter being probably located in the film layers close to the glass substrate. This process was suppressed in the case of FTO-coated glass substrates since the FTO layer (thickness  $\sim 550$  nm) prevented the direct  $\text{Na}^+$  diffusion into the  $\text{MnO}_x$  film. To definitively prove the role of  $\text{Na}^+$  cations in the stabilization of hollandite-type  $\text{MnO}_2$ , thermal annealing in air at  $500^\circ\text{C}$  was performed on a  $\text{MnO}_x$  film grown at 10 Pa of  $\text{O}_2$  on Si and in the presence of a  $20\ \mu\text{L}$  droplet of  $\text{Na}_2\text{SO}_4$  aqueous solution (only a circumscribed region of the sample was covered by the liquid). After rinsing the sample with deionized water to remove any trace of soluble sulphates, Raman spectroscopy confirmed the formation of  $\alpha\text{-MnO}_2$  in the region close to the droplet, while crystallization to the expected bixbyite  $\alpha\text{-Mn}_2\text{O}_3$  took place everywhere else (Fig. S14 in the Supplemental Material [44]). Moreover, clear morphology differences were revealed by SEM [Figs. 11(b) and 11(c)]: The region corresponding to  $\alpha\text{-MnO}_2$  comprises elongated rod-shaped crystals, while nanocrystalline grains (like those depicted in Fig. 4) are observed in the external  $\alpha\text{-Mn}_2\text{O}_3$  areas. EDXS analysis presented in Fig. S15 of the Supplemental Material [44] emphasizes the spatial distribution of  $\text{Na}^+$  cations and further proves that  $\alpha\text{-MnO}_2$  areas are enriched with Na. These findings are consistent with previous works about the selectivity of alkali-stabilized  $\text{MnO}_2$  phases during the crystallization pathways of  $\text{MnO}_2$  polymorphs in the presence of specific metal cations [97,98] and agree with the conclusions of Ref. [19], stating that single-crystal alkali-metal halide substrates provide dopant elements during  $\text{MnO}_2$  growth by ALD.

## V. CONCLUSIONS

In this paper, we described an efficient synthesis route—based on PLD followed by a proper thermal treatment either in oxidizing or reducing environment—to grow  $\text{MnO}_x$  thin films with the desired phase (e.g.,  $\text{MnO}$ ,  $\text{Mn}_3\text{O}_4$ ,  $\alpha\text{-Mn}_2\text{O}_3$ ,  $\text{A-MnO}_2$ ) and with tailored structural/morphological properties. The optimization of PLD and annealing parameters (mostly the  $\text{O}_2$  deposition pressure and the background atmosphere during postdeposition heating) allowed us to explore

different regions of the Mn–O phase diagram and to decouple the film morphology from its phase. As a result, several films exhibiting a wide range of porosity, thickness, crystallinity, and micro- and nanostructure could be obtained starting from the same  $\text{MnO}$  target, which could lead to a material with additional functional properties in view of electrochemical, catalytic, or sensing applications. Furthermore, we provided an extensive structural and phase characterization of as-deposited and annealed  $\text{MnO}_x$  thin films by means of Raman spectroscopy, emphasizing the phase transformations and the influence of  $\text{O}_2$  pressure, crystallinity, and nanostructure on the spectral features of the material. The reliability of Raman results under the 532 nm laser beam was carefully assessed, and the optimal condition for safe acquisition was identified. We corroborated the phase assignment from Raman spectroscopy by EDXS, XPS, and XRD measurements, providing additional details about the compositional properties, the Mn chemical state, and the crystalline texture of the films. Finally, we presented a peculiar case about the stabilization of  $\alpha\text{-MnO}_2$  phase exploiting the solid-state interdiffusion of  $\text{Na}^+$  cations during high-temperature air annealing of amorphous  $\text{MnO}_x$  films. Consequently, specifically designed substrates capable of providing dopant elements to the growing film may represent a successful strategy for the controlled stabilization and functionalization of metal-inserted  $\text{MnO}_x$  phases of technological interest. We envisage that further deposition and annealing conditions will contribute to the rationalization of the structural-morphological behavior of  $\text{MnO}_x$  thin films.

## ACKNOWLEDGMENTS

The Ph.D. scholarship of A. Macrelli and part of this paper pertain to the Energy for Motion project of the Department of Energy of Politecnico di Milano, funded by the Italian Ministry of Education, University, and Research (MIUR) through the Department of Excellence grant 2018–2022. A.L.B., V.R., and C.S.C. acknowledge funding under the National Recovery and Resilience Plan (NRRP), Mission 4 Component 2 Investment 1.3—Call for Tender No. 1561 of 11.10.2022 of Ministry of University and Research (MUR); the European Union—NextGenerationEU Award No. Project code PE0000021, Concession Decree No. 1561 of 11.10.2022 adopted by MUR, No. CUP D43C22003090001, Project title “Network 4 Energy Sustainable Transition—NEST.”

- 
- [1] C. M. Julien and A. Mauger, Nanostructured  $\text{MnO}_2$  as electrode materials for energy storage, *Nanomaterials* **7**, 396 (2017).
- [2] Y. Dessie, S. Tadesse, R. Eswaramoorthy, and B. Abebe, Recent developments in manganese oxide based nanomaterials with oxygen reduction reaction functionalities for energy conversion and storage applications: A review, *J. Sci.: Adv. Mater. Dev.* **4**, 353 (2019).
- [3] D. M. Robinson, Y. B. Go, M. Mui, G. Gardner, Z. Zhang, D. Mastrogiovanni, E. Garfunkel, J. Li, M. Greenblatt, and G. C. Dismukes, Photochemical water oxidation by crystalline polymorphs of manganese oxides: Structural requirements for catalysis, *J. Am. Chem. Soc.* **135**, 3494 (2013).
- [4] V. Mathew, B. Sambandam, S. Kim, S. Kim, S. Park, S. Lee, M. H. Alfuruqi, V. Soundharrajan, S. Islam, D. Y. Putro *et al.*, Manganese and vanadium oxide cathodes for aqueous rechargeable zinc-ion batteries: A focused view on performance, mechanism, and developments, *ACS Energy Lett.* **5**, 2376 (2020).
- [5] C. M. Julien, M. Massot, and C. Poinignon, Lattice vibrations of manganese oxides: Part I. Periodic structures, *Spectrochim. Acta A* **60**, 689 (2004).



- [6] S. Bernardini, F. Bellatreccia, A. Casanova Municchia, G. Della Ventura, and A. Sodo, Raman spectra of natural manganese oxides, *J. Raman Spectrosc.* **50**, 873 (2019).
- [7] Y. Xin, H. Cao, C. Liu, J. Chen, P. Liu, Y. Lu, and Z. Ling, A systematic spectroscopic study of laboratory synthesized manganese oxides relevant to Mars, *J. Raman Spectrosc.* **53**, 340 (2022).
- [8] C. B. Azzoni, M. C. Mozzati, P. Galinetto, A. Paleari, V. Massarotti, D. Capsoni, and M. Bini, Thermal stability and structural transition of metastable  $Mn_5O_8$ : *In situ* micro-Raman study, *Solid State Commun.* **112**, 375 (1999).
- [9] J. E. Post, D. A. McKeown, and P. J. Heaney, Raman spectroscopy study of manganese oxides: Tunnel structures, *Am. Mineral.* **105**, 1175 (2020).
- [10] J. E. Post, D. A. McKeown, and P. J. Heaney, Raman spectroscopy study of manganese oxides: Layer structures, *Am. Mineral.* **106**, 351 (2021).
- [11] F. Buciuman, F. Patcas, R. Craciun, and D. R. T. Zahn, Vibrational spectroscopy of bulk and supported manganese oxides, *Phys. Chem. Chem. Phys.* **1**, 185 (1998).
- [12] M.-C. Bernard, A. Hugot-Le Goff, B. V. Thi, and S. Cordoba de Torresi, Electrochromic reactions in manganese oxides I. Raman analysis, *J. Electrochem. Soc.* **140**, 3065 (1993).
- [13] M. A. Borysiewicz, M. Wzorek, M. Myśliwiec, J. Kaczmarski, and M. Ekielski,  $MnO_2$  ultrathin films deposited by means of magnetron sputtering: Relationships between process conditions, structural properties and performance in transparent supercapacitors, *Superlattices Microstruct.* **100**, 1213 (2016).
- [14] P. Fau, J. P. Bonino, and A. Rousset, Electrical properties of sputtered  $MnO_2$  thin films, *Appl. Surf. Sci.* **78**, 203 (1994).
- [15] H. D. Dawoud, T. Al Tahtamouni, and N. Bensalah, Sputtered manganese oxide thin film on carbon nanotubes sheet as a flexible and binder-free electrode for supercapacitors, *Int. J. Energy Res.* **43**, 1245 (2019).
- [16] O. Nilsen, H. Fjellvåg, and A. Kjekshus, Growth of manganese oxide thin films by atomic layer deposition, *Thin Solid Films* **444**, 44 (2003).
- [17] H. Jin, D. Hagen, and M. Karppinen, Low-temperature atomic layer deposition of crystalline manganese oxide thin films, *Dalton Trans.* **45**, 18737 (2016).
- [18] Y. W. Li, Q. Qiao, J. Z. Zhang, Z. G. Hu, and J. H. Chu, Influence of post-annealing on structural, electrical and optical properties of manganese oxide thin films grown by atomic layer deposition, *Thin Solid Films* **574**, 115 (2015).
- [19] O. Nilsen, S. Foss, H. Fjellvåg, and A. Kjekshus, Effect of substrate on the characteristics of manganese(IV) oxide thin films prepared by atomic layer deposition, *Thin Solid Films* **468**, 65 (2004).
- [20] A. A. Dakhel, Correlated structural and electrical properties of thin manganese oxide films, *Thin Solid Films* **496**, 353 (2006).
- [21] M. F. Al-Kuhaili, Chemical and optical properties of thermally evaporated manganese oxide thin films, *J. Vac. Sci. Technol. A* **24**, 1746 (2006).
- [22] W. Neubeck, L. Ranno, M. B. Hunt, C. Vettier, and D. Givord, Epitaxial  $MnO$  thin films grown by pulsed laser deposition, *Appl. Surf. Sci.* **138**, 195 (1999).
- [23] D. Yang, Pulsed laser deposition of manganese oxide thin films for supercapacitor applications, *J. Power Sources* **196**, 8843 (2011).
- [24] H. Xia, Y. Wan, F. Yan, and L. Lu, Manganese oxide thin films prepared by pulsed laser deposition for thin film microbatteries, *Mater. Chem. Phys.* **143**, 720 (2014).
- [25] S. Isber, E. Majdalani, M. Tabbal, T. Christidis, K. Zahraman, and B. Nsouli, Study of manganese oxide thin films grown by pulsed laser deposition, *Thin Solid Films* **517**, 1592 (2009).
- [26] L. M. Garten, P. Selvarasu, J. Perkins, D. Ginley, and A. Zakutayev, Phase formation of manganese oxide thin films using pulsed laser deposition, *Mater. Adv.* **2**, 303 (2021).
- [27] J. D. A. Pereira, J. N. Lacerda, I. F. Coelho, C. D. S. C. Nogueira, D. F. Franceschini, E. A. Ponzio, F. B. Mainier, and Y. Xing, Tuning the morphology of manganese oxide nanostructures for obtaining both high gravimetric and volumetric capacitance, *Mater. Adv.* **1**, 2433 (2020).
- [28] M. A. Dahamni, M. Ghamnia, S. E. Naceri, C. Fauquet, D. Tonneau, J. J. Pireaux, and A. Bouadi, Spray pyrolysis synthesis of pure and Mg-doped manganese oxide thin films, *Coatings* **11**, 598 (2021).
- [29] A. R. Merritt, R. Rajagopalan, and J. D. Carter, Synthesis of electro-active manganese oxide thin films by plasma enhanced chemical vapor deposition, *Thin Solid Films* **556**, 28 (2014).
- [30] L. W. Guo, D. L. Peng, H. Makino, T. Hanada, S. K. Hong, K. Sumiyama, T. Yao, and K. Inaba, Structural characteristics and magnetic properties of  $\lambda$ - $MnO_2$  films grown by plasma-assisted molecular beam epitaxy, *J. Appl. Phys.* **90**, 351 (2001).
- [31] S. Ching, S. M. Hughes, T. P. Gray, and E. J. Welch, Manganese oxide thin films prepared by nonaqueous sol-gel processing: Preferential formation of birnessite, *Microporous Mesoporous Mater.* **76**, 41 (2004).
- [32] S.-C. Pang, M. A. Anderson, and T. W. Chapman, Novel electrode materials for thin-film ultracapacitors: Comparison of electrochemical properties of sol-gel-derived and electrodeposited manganese dioxide, *J. Electrochem. Soc.* **147**, 444 (2000).
- [33] B. S. Singu and K. R. Yoon, Porous manganese oxide nanospheres for pseudocapacitor applications, *J. Alloys Compd.* **695**, 771 (2017).
- [34] A. Achour, A. Guerra, F. Moulai, M. Islam, T. Hadjersi, I. Ahmad, S. Parvez, R. Boukherroub, and J. J. Pireaux,  $MnO_x$  thin film based electrodes: Role of surface point defects and structure towards extreme enhancement in specific capacitance, *Mater. Chem. Phys.* **242**, 122487 (2020).
- [35] R. Cestaro, P. Schweizer, L. Philippe, X. Maeder, and A. Serrà, Phase and microstructure control of Electrodeposited Manganese Oxide with enhanced optical properties, *Appl. Surf. Sci.* **580**, 152289 (2022).
- [36] M. Tabbal, M. Abi-Akl, S. Isber, E. Majdalani, and T. Christidis, Synthesis of nano-grained  $MnO_2$  thin films by laser ablation, in: Laser Applications in Microelectronic and Optoelectronic Manufacturing VII, *SPIE* **7201**, 720104 (2009).
- [37] M. Abi-Akl, M. Tabbal, and W. Kassem, Crystalline phase control and growth selectivity of  $\beta$ - $MnO_2$  thin films by remote plasma assisted pulsed laser deposition, *Thin Solid Films* **612**, 450 (2016).
- [38] A. Macrelli, M. Olivieri, A. Lamperti, V. Russo, B. Bozzini, M. Menegazzo, G. Bussetti, C. S. Casari, and A. Li Bassi, Nanostructured  $Zn_xMn_{3-x}O_4$  thin films by pulsed laser deposition: A spectroscopic and electrochemical study towards the application in aqueous Zn-ion batteries, *Electrochim. Acta* **442**, 141909 (2023).

- [39] B. R. Bricchi, L. Mascaretti, S. Garattoni, M. Mazza, M. Ghidelli, A. Naldoni, and A. Li Bassi, Nanoporous titanium (oxy)nitride films as broadband solar absorbers, *ACS Appl. Mater. Interfaces* **14**, 18453 (2022).
- [40] G. Berti, A. Calloni, A. Brambilla, G. Bussetti, L. Duò, and F. Ciccacci, Direct observation of spin-resolved full and empty electron states in ferromagnetic surfaces, *Rev. Sci. Instrum.* **85**, 073901 (2014).
- [41] A. J. Nelson, J. G. Reynolds, and J. W. Roos, Core-level satellites and outer core-level multiplet splitting in Mn model compounds, *J. Vac. Sci. Technol. A* **18**, 1072 (2000).
- [42] S. Tanuma, C. J. Powell, and D. R. Penn, Calculations of electron inelastic mean free paths, *Surf. Interface Anal.* **21**, 165 (1993).
- [43] L. Lutterotti, MAUD: A Rietveld analysis program designed for the internet and experiment integration, *Acta Crystallogr. A* **56**, 54 (2000).
- [44] See Supplemental Material at <http://link.aps.org/supplemental/10.1103/PhysRevMaterials.7.083403> for a critical comparison of the main Raman peaks of several manganese oxides from previous literature sources, additional Raman spectra (MnO target; effect of incident laser power; 50 and 100 Pa samples after annealing supplied with tables; films on soda-lime glass and FTO-coated glass slides; effect of Na<sup>+</sup> cations) and XRD patterns (powder reference patterns of Mn oxide phases; full Rietveld refinement; MnO film; film on glass), additional SEM images, the UV-Vis optical curves, and selected EDXS spectra/maps of films in the presence of Na<sup>+</sup> cations.
- [45] N. Mironova-Ulmane, A. Kuzmin, and M. Grube, Raman and infrared spectromicroscopy of manganese oxides, *J. Alloys Compd.* **480**, 97 (2009).
- [46] N. Mironova-Ulmane, A. Kuzmin, V. Skvortsova, G. Chikvaidze, I. Sildos, J. Grabis, D. Jankoviča, A. Dindune, and M. Maiorov, Synthesis and vibration spectroscopy of nano-sized manganese oxides, *Acta Phys. Pol. A* **133**, 1013 (2018).
- [47] I. Rusakova, T. Ould-Ely, C. Hofmann, D. Prieto-Centurión, C. S. Levin, N. J. Halas, A. Lüttge, and K. H. Whitmire, Nanoparticle shape conservation in the conversion of MnO nanocrosses into Mn<sub>3</sub>O<sub>4</sub>, *Chem. Mater.* **19**, 1369 (2007).
- [48] F. Kapteijn, A. D. van Langeveld, J. A. Moulijn, A. Andreïni, M. A. Vuurman, A. M. Turek, J.-M. Jehng, and I. E. Wachs, Alumina-supported manganese oxide catalysts. I. Characterization: Effect of precursor and loading, *J. Catal.* **150**, 94 (1994).
- [49] A. Diallo, N. Tandjigora, S. Ndiaye, T. Jan, I. Ahmad, and M. Maaza, Green synthesis of single phase hausmannite Mn<sub>3</sub>O<sub>4</sub> nanoparticles via *Aspalathus linearis* natural extract, *SN Appl. Sci.* **3**, 562 (2021).
- [50] L. Malavasi, P. Galinetto, M. C. Mozzati, C. B. Azzoni, and G. Flor, Raman spectroscopy of AMn<sub>2</sub>O<sub>4</sub> (A = Mn, Mg and Zn) spinels, *Phys. Chem. Chem. Phys.* **4**, 3876 (2002).
- [51] H. D. Lutz, B. Müller, and H. J. Steiner, Lattice vibration spectra. LIX. Single crystal infrared and Raman studies of spinel type oxides, *J. Solid State Chem.* **90**, 54 (1991).
- [52] T. Gao, H. Fjellvåg, and P. Norby, A comparison study on Raman scattering properties of  $\alpha$ - and  $\beta$ -MnO<sub>2</sub>, *Anal. Chim. Acta* **648**, 235 (2009).
- [53] S. Ma, X. Ye, X. Jiang, W. Cen, W. Jiang, and H. Wang, First principles calculation of mechanical, dynamical and thermodynamic properties of MnO<sub>2</sub> with four crystal phases, *J. Alloys Compd.* **852**, 157007 (2021).
- [54] M. Sun, B. Lan, T. Lin, G. Cheng, F. Ye, L. Yu, X. Cheng, and X. Zheng, Controlled synthesis of nanostructured manganese oxide: Crystalline evolution and catalytic activities, *CrystEngComm* **15**, 7010 (2013).
- [55] Y. Xie, Y. Yu, X. Gong, Y. Guo, Y. Guo, Y. Wang, and G. Lu, Effect of the crystal plane figure on the catalytic performance of MnO<sub>2</sub> for the total oxidation of propane, *CrystEngComm* **17**, 3005 (2015).
- [56] C. M. Julien, M. Massot, S. Rangan, M. Lemal, and D. Guyomard, Study of structural defects in  $\gamma$ -MnO<sub>2</sub> by Raman spectroscopy, *J. Raman Spectrosc.* **33**, 223 (2002).
- [57] C. M. Julien, M. Massot, R. Baddour-Hadjean, S. Franger, S. Bach, and J.-P. Pereira-Ramos, Raman spectra of birnessite manganese dioxides, *Solid State Ion.* **159**, 345 (2003).
- [58] M. T. Nguyen Dinh, C. C. Nguyen, T. L. Truong Vu, V. T. Ho, and Q. D. Truong, Tailoring porous structure, reducibility and Mn<sup>4+</sup> fraction of  $\epsilon$ -MnO<sub>2</sub> microcubes for the complete oxidation of toluene, *Appl. Catal. A: Gen.* **595**, 117473 (2020).
- [59] R. Baddour-Hadjean and J.-P. Pereira-Ramos, Raman microspectrometry applied to the study of electrode materials for lithium batteries, *Chem. Rev.* **110**, 1278 (2010).
- [60] J. Lee, J. B. Ju, W. il Cho, B. W. Cho, and S. H. Oh, Todorokite-type MnO<sub>2</sub> as a zinc-ion intercalating material, *Electrochim. Acta* **112**, 138 (2013).
- [61] T. Gao, P. Norby, F. Krumeich, H. Okamoto, R. Nesper, and H. Fjellvåg, Synthesis and properties of layered-structured Mn<sub>5</sub>O<sub>8</sub> nanorods, *J. Phys. Chem. C* **114**, 922 (2010).
- [62] S. K. Ghosh, Diversity in the family of manganese oxides at the nanoscale: From fundamentals to applications, *ACS Omega* **5**, 25493 (2020).
- [63] J. E. Post, Manganese oxide minerals: Crystal structures and economic and environmental significance, *Proc. Natl. Acad. Sci. USA* **96**, 3447 (1999).
- [64] D. Gosztola and M. J. Weaver, Electroinduced structural changes in manganese dioxide + manganese hydroxide films as characterized by real-time surface-enhanced Raman spectroscopy, *J. Electroanal. Chem.* **271**, 141 (1989).
- [65] M. Tortosa, F. J. Manjón, M. Mollar, and B. Marí, ZnO-based spinels grown by electrodeposition, *J. Phys. Chem. Solids* **73**, 1111 (2012).
- [66] T. Larbi, K. Doll, and T. Manoubi, Density functional theory study of ferromagnetically and ferrimagnetically ordered spinel oxide Mn<sub>3</sub>O<sub>4</sub>. A quantum mechanical simulation of their IR and Raman spectra, *J. Alloys Compd.* **688**, 692 (2016).
- [67] E. Cockayne, I. Levin, H. Wu, and A. Llobet, Magnetic structure of bixbyite  $\alpha$ -Mn<sub>2</sub>O<sub>3</sub>: A combined DFT+*U* and neutron diffraction study, *Phys. Rev. B* **87**, 184413 (2013).
- [68] M. Regulski, R. Przeniosło, I. Sosnowska, D. Hohlwein, and R. Schneider, Neutron diffraction study of the magnetic structure of  $\alpha$ -Mn<sub>2</sub>O<sub>3</sub>, *J. Alloys Compd.* **362**, 236 (2004).
- [69] W. B. White and V. G. Keramidas, Vibrational spectra of oxides with the C-type rare earth oxide structure, *Spectrochim. Acta A* **28**, 501 (1972).
- [70] S. Bernardini, F. Bellatreccia, G. Della Ventura, and A. Sodo, A reliable method for determining the oxidation state of manganese at the microscale in Mn oxides *via* Raman spectroscopy, *Geostand. Geoanal. Res.* **45**, 223 (2021).

- [71] C. S. Casari and A. Li Bassi, Pulsed laser deposition of nanostructured oxides: From clusters to functional films, in *Advances in Laser and Optics Research*, edited by W. T. Arkin (Nova Science Publishers, Inc., 2011), Vol. 7, pp. 65–100.
- [72] A. Bailini, F. Di Fonzo, M. Fusi, C. S. Casari, A. Li Bassi, V. Russo, A. Baserga, and C. E. Bottani, Pulsed laser deposition of tungsten and tungsten oxide thin films with tailored structure at the nano- and mesoscale, *Appl. Surf. Sci.* **253**, 8130 (2007).
- [73] R. Ghosh, M. K. Brennaman, T. Uher, M. R. Ok, E. T. Samulski, L. E. McNeil, T. J. Meyer, and R. Lopez, Nanoforest Nb<sub>2</sub>O<sub>5</sub> photoanodes for dye-sensitized solar cells by pulsed laser deposition, *ACS Appl. Mater. Interfaces* **3**, 3929 (2011).
- [74] P. Gondoni, P. Mazzolini, V. Russo, M. Diani, M. Amati, L. Gregoratti, V. De Renzi, G. C. Gazzadi, J. Martí-Rujas, A. Li Bassi *et al.*, Tuning electrical properties of hierarchically assembled Al-doped ZnO nanoforests by room temperature pulsed laser deposition, *Thin Solid Films* **594**, 12 (2015).
- [75] R. Matarrese, I. Nova, A. Li Bassi, C. S. Casari, V. Russo, and S. Palmas, Preparation and optimization of TiO<sub>2</sub> photoanodes fabricated by pulsed laser deposition for photoelectrochemical water splitting, *J. Solid State Electrochem.* **21**, 3139 (2017).
- [76] S. Bernardini, F. Bellatreccia, G. Della Ventura, P. Ballirano, and A. Sodo, Raman spectroscopy and laser-induced degradation of groutelite and ramsdellite, two cathode materials of technological interest, *RSC Adv.* **10**, 923 (2020).
- [77] S. Fritsch and A. Navrotsky, Thermodynamic properties of manganese oxides, *J. Am. Ceram. Soc.* **79**, 1761 (1996).
- [78] E. Biserni, A. Scarpellini, R. Brescia, D. Dellasega, A. Li Bassi, and P. Bruno, Room temperature fabrication of silicon nanocrystals by pulsed laser deposition, *J. Nanopart. Res.* **16**, 2461 (2014).
- [79] M. C. Biesinger, B. P. Payne, A. P. Grosvenor, L. W. M. Lau, A. R. Gerson, and R. S. C. Smart, Resolving surface chemical states in XPS analysis of first row transition metals, oxides and hydroxides: Cr, Mn, Fe, Co and Ni, *Appl. Surf. Sci.* **257**, 2717 (2011).
- [80] E. S. Ilton, J. E. Post, P. J. Heaney, F. T. Ling, and S. N. Kerisit, XPS determination of Mn oxidation states in Mn (hydr)oxides, *Appl. Surf. Sci.* **366**, 475 (2016).
- [81] J. L. Junta and M. F. Hochella Jr., Manganese (II) oxidation at mineral surfaces: A microscopic and spectroscopic study, *Geochim. Cosmochim. Acta* **58**, 4985 (1994).
- [82] M. A. Stranick, MnO<sub>2</sub> by XPS, *Surf. Sci. Spectra* **6**, 31 (1999).
- [83] M. A. Stranick, Mn<sub>2</sub>O<sub>3</sub> by XPS, *Surf. Sci. Spectra* **6**, 39 (1999).
- [84] C. S. Fadley, D. A. Shirley, A. J. Freeman, P. S. Bagus, and J. V. Mallow, Multiplet Splitting of Core-Electron Binding Energies in Transition-Metal Ions, *Phys. Rev. Lett.* **23**, 1397 (1969).
- [85] M. Chigane and M. Ishikawa, Manganese oxide thin film preparation by potentiostatic electrolyses and electrochromism, *J. Electrochem. Soc.* **147**, 2246 (2000).
- [86] M. Toupin, T. Brousse, and D. Bélanger, Charge storage mechanism of MnO<sub>2</sub> electrode used in aqueous electrochemical capacitor, *Chem. Mater.* **16**, 3184 (2004).
- [87] A. V. Chichagov, D. A. Varlamov, R. A. Dilanyan, T. N. Dokina, N. A. Drozhzhina, O. L. Samokhvalova, and T. V. Ushakovskaya, MINCRYST: A crystallographic database for minerals, local and network (WWW) versions, *Crystallogr. Rep.* **46**, 876 (2001).
- [88] R. T. Downs and M. Hall-Wallace, The American Mineralogist Crystal Structure Database, *Am. Mineral.* **88**, 247 (2003).
- [89] WWW-MINCRYST (2023). Crystallographic and crystallochemical database for minerals and their structural analogues. Card No. 1876: Hausmannite, [http://database.iem.ac.ru/mincryst/s\\_carta.php?1876](http://database.iem.ac.ru/mincryst/s_carta.php?1876).
- [90] M. Birkholz, P. F. Fewster, and C. Genzel, *Thin Film Analysis by X-Ray Scattering* (Wiley-VCH Verlag GmbH & Co., KGaA, Weinheim, 2006).
- [91] I. Levin, NIST Inorganic Crystal Structure Database (ICSD), National Institute of Standards and Technology (2018).
- [92] D. Jarosch, Crystal structure refinement and reflectance measurements of hausmannite, Mn<sub>3</sub>O<sub>4</sub>, *Mineral. Petrol.* **37**, 15 (1987).
- [93] H. Xu, S. Xu, H. Wang, and H. Yan, Characterization of hausmannite Mn<sub>3</sub>O<sub>4</sub> thin films by chemical bath deposition, *J. Electrochem. Soc.* **152**, C803 (2005).
- [94] WWW-MINCRYST (2023). Crystallographic and crystallochemical database for minerals and their structural analogues. Card No. 5956: Bixbyite, [http://database.iem.ac.ru/mincryst/s\\_carta.php?5956](http://database.iem.ac.ru/mincryst/s_carta.php?5956).
- [95] WWW-MINCRYST (2023). Crystallographic and crystallochemical database for minerals and their structural analogues. Card No. 6307: Manganosite, [http://database.iem.ac.ru/mincryst/s\\_carta.php?6307](http://database.iem.ac.ru/mincryst/s_carta.php?6307).
- [96] Paul Marienfeld GmbH & Co. KG, Chemical and physical properties. Microscope slides made of soda lime glass of the 3<sup>rd</sup> hydrolytic class, <https://www.marienfeld-superior.com/anleitungen-2610.html?file=files/Medien/PDFs/Technische%20Informationen/DE/Datenblatt-Objekttraeger-EN.pdf&cid=75634>.
- [97] D. A. Kitchaev, S. T. Dacek, W. Sun, and G. Ceder, Thermodynamics of phase selection in MnO<sub>2</sub> framework structures through alkali intercalation and hydration, *J. Am. Chem. Soc.* **139**, 2672 (2017).
- [98] B. R. Chen, W. Sun, D. A. Kitchaev, J. S. Mangum, V. Thampy, L. M. Garten, D. S. Ginley, B. P. Gorman, K. H. Stone, G. Ceder *et al.*, Understanding crystallization pathways leading to manganese oxide polymorph formation, *Nat. Commun.* **9**, 2553 (2018).